GALLOPING OF A BUNDLED CONDUCTOR TRANSMISSION LINE

BY

QINGXIN ZHANG

A THESIS SUBMITTED TO THE FACULTY OF GRADUATE STUDIES
IN PARTIAL FULFILLMENT OF
THE REQUIREMENTS FOR THE DEGREE OF
MASTER OF SCIENCE

DEPARTMENT OF CIVIL & GEOLOGICAL ENGINEERING

UNIVERSITY OF MANITOBA

WINNIPEG, MANITOBA

THE UNIVERSITY OF MANITOBA

FACULTY OF GRADUATE STUDIES

*****

COPYRIGHT PERMISSION PAGE

Galloping of a Bundled Conductor Transmission Line

BY

Qingxin Zhang

A Thesis/Practicum submitted to the Faculty of Graduate Studies of The University of Manitoba in partial fulfillment of the requirements of the degree of Master of Science

Abstract

A useful design tool is developed for a bundle conductor or a single conductor of an electrical transmission line by using a three-degree-of-freedom, hybrid model. The model is adaptable because it incorporates numerical mode shapes determined by employing the finite element technique to form relevant matrices. On the other hand, it is quite computationally efficient because analytical expressions are used to investigate the initiation and steady-state amplitudes of galloping. The model accommodates not only interactions of the vertical, horizontal and torsional movements but also non-linear aerodynamic loads, a non-uniform ice geometry, and distributed and discrete galloping control devices that cannot be considered in existing analytical models. By neglecting the sub-span motions between the conductors, a bundle is modelled as an equivalent single conductor so that the initiation conditions for galloping, periodic and quasi-periodic states and their stability conditions are considered by taking advantage of previous achievements for a single conductor. Numerical examples are presented to assess the accuracy of the results obtained from the model in comparison with analogous data from a more sophisticated finite element analysis. Parametric studies are reported for limit cycle amplitudes with variations of the critical wind speed, wind speed above the critical wind speed, static tension and span length. Finally, the model is used to assess the effects of a hybrid, control damper to alleviate galloping by changing its parameters and providing guidelines for its application.

Acknowledgements

The author would like to express his deep gratitude to his thesis advisors Drs. A. H. Shah and N. Popplewell for guiding this project and providing invaluable academic support. Sincere thanks are extended to Drs. P. Yu, Y. M. Desai and M. Liao for their computer programs used in a single conductor and a twin bundle. The helpful discussions with Mr. M. Lu and his assistance in providing a control device's data are also appreciated greatly.

The financial support from Manitoba Hydro and the research grants of Profs. A. H. Shah and N. Popplewell are acknowledged gratefully.

Table of Contents

List of Tables

List of Figures

Chapter 1

INTRODUCTION

1.1 Background

Overhead electrical transmission lines consist of single or bundled conductors. Electrical power utilities are often faced with wind-induced conductor motion in the form of aeolian vibration, conductor gallop and wake-induced oscillation. Wake-induced oscillation, which is peculiar to bundled conductors, arises from the shielding effect by windward subconductors on leeward ones. Its frequency range is about 0.15 to 10 Hz and the maximum amplitude approximates 80 multiples of the conductor's diameter. Aeolian vibration and conductor galloping are observed on single as well as bundled conductors. Aeolian vibration is caused by an alternating pressure unbalance which is created by the alternate shedding of wind-induced vortices from the top and bottom sides of the conductor. The amplitude of aeolian vibration can be up to the order of the conductor's diameter at a high (10 to 100Hz) frequency. Compared to aeolian vibration, galloping is characterized by a low frequency (0.1 to 3Hz), large amplitude (5 to 300 multiples of the conductor's diameter), self-excited oscillation. It is produced by aerodynamic instabilities which stem from asymmetry in a conductor's cross section due to ice accretion or, more rarely, from the stranding of the conductor itself.

Different behaviors of these three motions produce different types of damage to transmission line system. Galloping is considered because its large amplitude of motion induces high dynamic loads. Damage caused by galloping usually occurs in approximately 1 to 48 hours if vibrations are sustained compared to a longer 3 month to more than 20 year period when aeolian vibration prevails. Galloping cannot only break conductor strands, but it can damage dampers, tie-wires, insulator pins, suspension hardware, crossarm hardware, poles and towers. In addition, forced

outages caused by galloping result in loss of revenue and sometimes in other costs associated with reestablishing service. These penalties are generally considered to be greater than those from direct damage to lines. Therefore, this thesis is limited only to galloping.

1.2 Literature review

A theoretical investigation of galloping can be categorized generally as analytical or numerical, regardless of the configuration of the conductors. Analytical techniques provide global trends while numerical approaches are used to study specific interactions. Although the present theoretical studies give a fundamental knowledge for understanding the galloping of transmission lines, additional work is needed to establish an adaptable model which can accommodate galloping control devices and be used to analyze the effects of a system's parameters. The scope of this literature survey emphasizes representative achievements of analytical methods and numerical simulations as well as the control of galloping.

1.2.1 Analytical methods

An analytical approach may include studies on the initiation of galloping or the resulting limit cycle amplitude. Usually, the initiation conditions for galloping are obtained by linearizing the nonlinear equations of motion near the conductor's static profile. In 1932, Den Hartog proposed an analytical single degree-of-freedom (DOF) model for galloping of a transmission line [1]. His model suggested that galloping may be initiated if the drag coefficient is less than the negative slope of the lift coefficient with respect to the relative aerodynamic angle of attack. The Den Hartog criterion, which only considers the vertical motion of a conductor, has been used widely. However, according to field observations [2], this simplest model neglects the importance of a conductor's torsional motion. It has been suggested that the twist of a conductor plays an important role in the initiation of galloping [3, 4, 5, 6, 7, 8, 9]. Some researchers emphasized that, according to wind tunnel experiments [5], the galloping of a naturally iced line is caused by a self-excited torsional motion rather than by a Den Hartog type of instability. Furthermore, a

horizontal motion, when coupled to a vertical (plunge) movement, can initiate vertical galloping [10, 11, 12]. A recent analysis has extended the simple theory to combined vertical, horizontal and torsional motions in order to determine the initiation of galloping [13, 14, 15]. In addition, several initiation studies also showed the use of geometric stability diagrams to assess the effectiveness of a system's parameters on the initiation of galloping [3, 16, 17, 18, 19].

The galloping amplitudes, frequencies and relative phase differences between vibrating components need to be determined if a transmission line's static equilibrium position is found to be unstable. Perturbation methods are usually used to find closed form solutions for periodic and quasi-periodic motions. For example, a Fourier series residual approximation was employed to determine the purely vertical, unimodal galloping amplitude [20], an asymptotic method was considered to give a closed form for a nonresonance [21], a time average technique was adapted to obtain analytical solutions of both an internal resonance and a nonresonance for the combined vertical and torsional motions [22] or vertical, torsional and horizontal vibrations [13, 14, 15]. Other analytical approaches, such as the decomposition of the nonlinear equations of motion [23], the generalized Galerkin method [24], the describing function method [25], have been also applied to galloping. Moreover, the stability conditions of limit cycles can be derived by bifurcation techniques [13, 15].

Bundle conductors have been used widely due to their economical large current -carrying capacity [2]. However, they gallop more easily than a single conductor. Most previous analytical studies of bundle conductors have been limited to a plannar configuration [12, 26, 27, 28, 29]. Although a 3DOF, analytical model has been formulated recently for a bundle conductor [30], a tedious time integration procedure was adopted and the aerodynamic forces were over simplified by their linearization. Until now, no analytical model (which includes analytical solutions for both an internal resonance and a nonresonance, initiation conditions and the stability of limit cycles) are available for a bundle conductor. On the other hand, an analytical approach can give global trends but it may overly simplify practical issues. For example, an analytical model cannot accommodate practically important non-uniformities arising, say, from icing variations

or localized control devices like airflow spoilers or detuning pendulums [13, 15].

1.2.2 Numerical simulation

Most numerical schemes are based on the discretization of the dynamic equilibrium equations. The finite element (FE) method has been often used to approximate spatial variables [31, 32, 33]. However, a numerically simulated growth to an eventual periodic state (often associated with galloping) requires disadvantageously protracted computations because transmission lines are very lightly damped at low frequencies. In addition, the existence of a periodic state is not known a priori so that computations may be fruitless. Especially, it is impractical for a numerical simulation to efficiently compute the effects of design changes caused by parameters like the static tension, the span length and the number of conductors in a bundle or the result of a greater wind speed.

Very few references have obtained the high computational efficiency needed for a numerical galloping simulation. Compared with traditional FE techniques, a FE model formulated recently for a single conductor can greatly reduce computer time by selecting the initial (time) conditions [13, 34]. It considered both internal resonance and nonresonance as well as stability analysis by using time average method. The model has been extended to a twin bundle conductor [35] . However, this approach presupposed that an approximate limit cycle may be obtained from a previous analytical solution.

1.2.3 Galloping control

The final objective in studying the galloping of iced, electrical transmission lines is to control the galloping itself. A variety of methods are currently in use or under field evaluation for protecting lines against galloping or its side effects. They include ice melting, increased clearances between conductors, interphase spacers, aerodynamic drag dampers, wind dampers, airflow spoilers and detuning pendulums.

The protection measure that was utilized earliest was the removal of ice, or preventing its

formation, by heating conductors electrically [36, 37]. Early applications of this method were apparently aimed at preventing failures due to the additional weight of ice on conductors, and faults resulting from the contact between phases or a phase and a ground wire when the sudden release of ice from a span caused "sleet jump". Galloping prevention by using ice melting has been the primary objective during the last several decades. However, there is conflict between providing enough resistance in the conductors to permit effective heating for melting the ice, on the one hand, and minimizing of year-round system losses on the other.

Increased clearances between phases and between phases and ground wires are applied widely to alleviate outages caused by galloping. The approach is based on determining limit cycle amplitudes (galloping ellipses) [38, 39] and experience to guide the clearance of transmission lines. Actually, an increased clearance cannot prevent galloping; it just passively lessens the damage produced by outages.

Some utilities often use interphase spacers to prevent phase-to-phase contacts. The device works effectively by restraining the relative motion between phases at the points in the span where the devices are located. Thus a line's galloping motion is forced into a mode in which flashovers are much less likely [40, 41, 42]. Interphase spacers also do not eliminate galloping. In fact, they can result in an ice shape that makes a conductor more prone to gallop as the interphase spacers prevent the free rotation of the conductor under the eccentric weight of the growing ice deposit.

Aerodynamic drag dampers augment the damping effect of a conductor's aerodynamic drag and, thus, they narrow the conditions under which lift forces may supply enough energy to sustain galloping. Although most analyses of the effectiveness of drag damping are based upon the Den Hartog mechanism, such dampers may have beneficial effects even when a torsional motion of the conductor is involved [42, 43, 44].

Detuning pendulums are aimed at controlling torsional motions with the object of reducing the incidence or intensity of galloping. Extensive field work has been done on this device in North America [27, 40, 41, 42, 45]. In general, a bare conductor has a high ratio of its

lowest torsional to vertical (plunge) natural frequencies. This frequency ratio can be reduced substantially by the aerodynamic moment acting on an iced conductor and by the "inverted pendulum effect" of the weight of the accreted ice. The attached pendulums counteract these effects and keep the torsional frequencies of the span well above the natural frequencies of the one-, two-, and three- loop, predominantly vertical modes. It was reported that detuning pendulums may reduce the average motion of a single as well as two and four conductor bundle lines during freezing rain events in North America [41, 42, 45]. Although detuning pendulums are used widely by utilities in North America, they cannot completely control galloping. One reason is that galloping may not be only dominated by a torsional movement.

Other control devices, like airflow spoilers [27, 40, 42] and wind dampers [27] etc., have not been used widely by utilities due to their limited effectiveness. It is very difficult to control the galloping of transmission lines because they have very light damping and they are exposed to all atmospheric conditions. Many researchers are trying to find a new device that effectively alleviates all types of galloping. Experimental development of such a device is very expensive. It is more cost effective to initially establish a computer model to assess the effectiveness of a new device before experiments are performed.

1.3 Objectives of this project

As stated in the previous section, an analytical approach cannot handle variations of structural damping and icing along a span while a numerical simulation needs disadvantageously protracted computations. Neither a purely numerical nor a purely analytical approach seems capable of conveniently describing galloping. An appropriate combination of these two methods is almost certainly required. One of the objectives of this thesis is to develop an adaptable but still computationally efficient, 3DOF model that uses FE mode shapes instead of their analytical counterparts. These mode shapes are then used in conjunction with analytical expressions [13, 15] to investigate the initiation and steady-state amplitude of galloping. The final model cannot only handle non-uniform icing variations along a span but it can also accommodate

localized control devices for a single conductor as well as a bundle having any number of conductors. The other objective is to develop a potential control device, a hybrid damper (HD), to alleviate the galloping and propose guidelines for the selection of its parameters.

1.4 Organization of thesis

This thesis is organized as follows. Chapter 1 gives a general description of the vibrations of a transmission line. The literature survey emphasizes analytical methods and numerical simulations as well as galloping control. The objectives and organization of this thesis are also given in this chapter. Chapter 2 reviews the mathematical method for galloping. General steps in studying galloping are presented for the initiation of galloping, limit cycles and their stability. Chapter 3 develops a 3DOF hybrid model that can handle a non-uniform variation of ice and accommodate control devices like an airflow spoiler or detuning pendulum. The model, which is based on previous achievement [13, 15], includes the initiation conditions of galloping and analytical solutions of both internal resonance and nonresonance for a single conductor and a bundle having any number of conductors . Examples are given not only to compare the results from the FE model but also to analyze the effects of design parameters like the static tension, the span length and the number of conductors in a bundle or a greater wind speed. Chapter 4 uses the modified 3DOF model to analyze the effects of the hybrid damper's parameters on galloping so that an optimum design can be assessed. Finally, conclusions are given in Chapter 5.

Chapter 2

MATHEMATICAL METHOD

2.1 Introduction

Transmission lines are lightly damped and susceptible to low frequency, large amplitude vibrations when aerodynamic loads act on them. The equation of motion used to describe the system are nonlinear due to the nonlinear aerodynamic forces. Protracted computation is needed if conventional time integration is used to find a solution. One reason is that the existence of a periodic solution is not known in advance and numerical simulation over a short time cannot display the complete picture of low frequency galloping. In addition, it is impractical to use time integration if a parameter analysis is required for the design of new lines and vibration control. Therefore, a method to substantially save computational time is definitely recommended.

A time average approach is one that transfers equations dependent on time to time-independent algebraic equations. Consequently, computational effort is reduced greatly [13, 14, 15, 22]. Not only can the periodic solutions of these equations be obtained conveniently but their stability conditions can also be given to determine whether the vibration amplitude will be sustained.

2.2 Governing equations and their solution

The equations of motion for a N DOF system generally have the form [13]

$$\mathbf{M}\ddot{\mathbf{q}} + \mathbf{C}\dot{\mathbf{q}} + \mathbf{K}\mathbf{q} = \mathbf{F} \tag{2.1}$$

where $\mathbf{M}, \mathbf{C}$ and $\mathbf{K}$ are the $N \times N$ structural mass, damping and stiffness matrices, respectively, and $\mathbf{F}$ is the external load vector. $\mathbf{q}$ is the generalized displacement vector. The system

described by equation (2.1) corresponds to an electric transmission line and it is autonomous and weakly nonlinear. Equation (2.1) can be transferred to a canonical form by using the traditional principal coordinate theory so that

$$\ddot{\eta}_i + \omega_i^2 \eta_i = \epsilon F_i(\eta_1, \eta_2, \cdots, \eta_l, \dot{\eta}_1, \dot{\eta}_2, \cdots, \dot{\eta}_m) \qquad l, m \leq N. \tag{2.2}$$

The η_i and ω_i are the ith principal coordinate and eigenvalue of the corresponding linear, undamped system (for which $\epsilon = 0$), respectively. The term ϵF_i, which represents the nonlinear aerodynamic and damping forces, are order ϵ ($\epsilon \ll 1$) in comparison to the inertial and elastic forces. In order to yield closed form periodic solutions, the Krylov-Bogoliubov (KB) technique is applied to the modified equations

$$\ddot{\eta}_i + \omega_i^{*^2} \eta_i = \epsilon F_i + (\omega_i^{*^2} - \omega_i^2)\eta_i, \qquad i = 1, 2, \ldots, N \tag{2.3}$$

instead of equation (2.2). The ω^* are unknown and $\mid \omega_i^* - \omega_i^2 \mid = O(\epsilon)$. Assume periodic solutions of the form

$$\eta_i(t) = A_i(t) \cos \Psi_i(t) \tag{2.4}$$

where

$$\Psi_i(t) = \omega_i^* t + \phi_i(t). \tag{2.5}$$

$A_i(t)$ and $\phi_i(t)$ are the ith amplitude and phase, respectively. Differentiate equation (2.4) with respect to t and let the amplitude and phase be chosen such that

$$\dot{\eta}_i(t) = -A_i(t)\omega_i^* \sin \Psi_i(t) \tag{2.6}$$

and

$$\dot{A}_i(t) \cos \Psi_i(t) - A_i(t)\dot{\phi}_i(t) \sin \Psi_i(t) = 0. \tag{2.7}$$

Then differentiate equation (2.6) again and substitute the resulting equation and equation (2.4) into equation (2.3) to produce

$$\dot{A}_i(t) \sin \Psi_i(t) + A_i(t)\dot{\phi}_i(t) \cos \Psi_i(t) = (\omega_i^2 - \omega_i^{*^2}) A_i(t) \cos \Psi_i(t) - \epsilon F_i. \tag{2.8}$$

By employing the KB method and algebraically manipulating equations (2.7) and (2.8), the following equations can be obtained

$$\omega_i^* \dot{A}_i(t) = \lim_{T\to\infty} \frac{1}{T} \int_0^T R_i(t) \sin \Psi_i(t) dt \qquad i = 1, 2, \cdots, N \tag{2.9}$$

and

$$\omega_i^* A_i(t) \dot{\phi}_i = \lim_{T\to\infty} \frac{1}{T} \int_0^T R_i(t) \cos \Psi_i(t) dt \qquad i = 1, 2, \cdots, N \tag{2.10}$$

where

$$R_i = (\omega_i^2 - \omega_i^{*^2})\eta_i - \epsilon F_i. \tag{2.11}$$

The slowly varying functions, $A_i(t)$ and $\phi_i(t)$ are effectively treated as constants in equations (2.9) and (2.10) when integrations are performed with respect to time, t. The A_i, ϕ_i and ω_i^* can be found by letting $\dot{A}_i = \dot{\phi}_i = 0$ in equations (2.9) and (2.10). Equation (2.4) gives the corresponding periodic and quasiperiodic solutions.

2.3 Initiation of galloping and stability of limit cycles

The initiation of galloping depends on the stability of the static equilibrium configuration of a transmission line. Galloping is initiated if a static configuration is unstable. The stability analysis is performed by linearizing equation (2.1), which is rewritten as

$$\mathbf{M}\ddot{\mathbf{q}} + \mathbf{C_L}\dot{\mathbf{q}} + \mathbf{K_L}\dot{\mathbf{q}} = \mathbf{F_H} \tag{2.12}$$

where

$$\mathbf{C_L} = \mathbf{C} - \mathbf{C_u} \qquad \mathbf{K_L} = \mathbf{K} - \mathbf{K_u}. \tag{2.13}$$

$\mathbf{C}_u$ and $\mathbf{K}_u$ are the linear terms produced from $\mathbf{F}$. $\mathbf{F_H}$ in equation (2.12) represents higher order terms of the aerodynamic loads. The characteristic matrix can be obtained from equation (2.12) as [46]

$$\mathbf{S}_{cs} = \begin{bmatrix} \mathbf{0} & \mathbf{I} \\ -\mathbf{M}^{-1}\mathbf{K}_L & -\mathbf{M}^{-1}\mathbf{C}_L \end{bmatrix} \tag{2.14}$$

where $\mathbf{0}$ and $\mathbf{I}$ are the $N \times N$ null and identity matrices, respectively. Galloping (i.e. the static configuration is unstable) occurs if at least one of the eigenvalues of $\mathbf{S}_{cs}$, λ, has a positive real part. The stability conditions can be found by applying the Routh-Hurwitz criteria to the characteristic polynomial

$$det(\mathbf{S}_{cs} - \lambda \mathbf{E}) = 0 \tag{2.15}$$

where $\mathbf{E}$ is the unit matrix of size $2N \times 2N$.

The stability of the steady states can be determined by the Jacobian matrix, $\mathbf{J}$, from equations (2.9) and (2.10). $\mathbf{J}$ has elements given by

$$\begin{cases} J_{i,j} = \frac{\partial \dot{A}_i}{\partial A_j} & i,j \leq N \\ J_{i,j} = \frac{\partial \dot{A}_i}{\partial \phi_l} & i \leq N,\ \ j = N+l,\ \ l = 1,2,\cdots,m \\ J_{i,j} = \frac{\partial \dot{\phi}_i}{\partial A_i} & i \geq N+l,\ \ j \leq N,\ \ l = 1,2,\cdots,m \\ J_{i,j} = \frac{\partial \dot{\phi}_i}{\partial \phi_k} & i = N+l,\ \ j = N+k,\ \ l,k = 1,2,\cdots,m \end{cases} \tag{2.16}$$

where m is the number of internally resonant modes. Similarly, the stability conditions of the limit cycles can be obtained by applying the Routh-Hurwitz criterion to the following characteristic polynomial

$$det(\mathbf{J} - \lambda \mathbf{E}) = 0. \tag{2.17}$$

Limit cycles are stable if all the real parts of the nonzero eigenvalues of equation (2.17) are negative.

Chapter 3

HYBRID MODEL

3.1 Introduction

As stated in Chapter 1, a 3DOF hybrid model is developed in this chapter by extending the approach used for a single conductor [13, 15] to a bundle configuration having any number of conductors. This model modifies the model used for a single conductor to accommodate non-uniform icing as well as control devices by adopting FE mode shapes.

Although an arbitrary number of conductors is considered, the particular example of a twin conductor bundle is illustrated in Fig.3.1 for simplicity. Fig.3.1(a) presents the static positions of the two conductors that are produced by the conductors' weights and tensions as well as by the steady (side) wind and the weight of accreted ice. A typical cross-section of the ith iced conductor (where i=1,2 for the twin bundle) is shown in Fig.3.1(b). Physical rigid spacers joining the conductors are illustrated as solid lines. Weightless, rigid fictitious spacers are introduced that periodically join the conductors to ensure that they essentially move together (i.e. the bulk motion constraint). Of course such spacers, which are represented in Fig.3.1(a) by dashed lines, are not needed for a single conductor. The reference curve for the bundle is considered to go through the mass center of each cross section of the bundle, as indicated in Fig.3.1(a). On the other hand, adjacent spans are always idealized, as for the single conductor, by equivalent linear springs. Therefore, the principal difference between the single and bundle conductor approaches is the advancement of fictitious spacers and a reference curve for a bundle configuration.

The hybrid model makes the following assumptions in order to extend the single conductor formulation to a bundle conductor.

1. Inertial and damping forces in the longitudinal direction, as well as the rotation of individual conductors about this direction, are neglected.

2. A line's sag-to-span ratio is small.

3. The rotation of the bundle about the reference curve is small so that the linearized theory can be employed and spacers are rigid.

4. No more than one mode per global direction is considered simultaneously.

5. The relative motions between the conductors of a bundle are neglected and the longitudinal motions of each of the conductors are presumed to be identical.

Items 1, 2 and 5 are the commonly made assumptions for the bulk motion of a bundle. The third item is reasonable in many cases because a bundle's torsional stiffness is much greater than that of a single conductor so that large rotations happen rarely. Item 4, on the other hand, presumes that the larger torsional stiffness of a bundle hardly changes the negligible coupling that is assumed for the single conductor for modes acting in the same direction. These simplifying assumptions are used next to formulate the hybrid model.

3.2 Displacement relationship

The dynamic displacement at an arbitrary point (s, y, z) of any one conductor in a bundle is measured from that point's static position. It is given by

$$\begin{aligned} u_X(s,y,z,t) &= U(s,t) \\ v_Y(s,y,z,t) &= V(s,t) - z\Theta(s,t) \\ w_Z(s,y,z,t) &= W(s,t) + y\Theta(s,t) \ . \end{aligned} \tag{3.1}$$

X, Y and Z are the global coordinates illustrated in Fig.3.1(a) while x, y and z are the local coordinates shown in Fig.3.1(b). The latter are off-set from the global coordinates and their origin is located on the reference curve at the left support. u_X, v_Y and w_Z are the global displacements at (s, y, z) and instant t. Their direction is indicated by the corresponding suffix. On the other hand, s is the intrinsic coordinate which indicates the distance that a cross section

of the bundle is from the reference curve's origin. U, V and W are the global displacements of any point of the reference curve in the X, Y and Z directions, respectively. Θ is the rotation of the bundle about the reference curve and it is assumed to be small. If only one mode is considered in each direction, then U, V, W and Θ can be expressed as

$$\begin{aligned} U(s,t) &= q_u(t) f_u(s) \\ V(s,t) &= q_v(t) f_v(s) \\ W(s,t) &= q_w(t) f_w(s) \\ \Theta(s,t) &= q_\theta(t) f_\theta(s) \ . \end{aligned} \tag{3.2}$$

The q_i and f_i, where $i = u, v, w, \theta$, are generalized coordinates and the associated mode shapes provided by the FE model, respectively. (See Section 3.4.) Furthermore, the displacements of the center of the ith conductor in the bundle, U_i, V_i and W_i, are described by

$$\begin{aligned} U_i(s,y,z,t) &= U(s,y,z,t) \\ V_i(s,y,z,t) &= V(s,t) - r_i \sin\theta_{i0}\Theta(s,t) \\ W_i(s,y,z,t) &= W(s,t) + r_i \cos\theta_{i0}\Theta(s,t) \ . \end{aligned} \tag{3.3}$$

Here r_i is the distance between the reference curve and the center of the ith bare conductor at the bundle's cross section of interest. Moreover, θ_{i0} is the initial clockwise angle of this conductor from the positive direction of the y axis, as illustrated in Fig.3.1(b).

3.3 Equations of motion

The equations of motion of the bundle are found by employing the conventional variational principle [47], i.e.

$$\int_{t_1}^{t_2} \delta(T_k - V_s)dt + \int_{t_1}^{t_2} \delta W_{nc} dt = 0 \tag{3.4}$$

where T_k and V_s are the total kinetic and strain energies, respectively. W_{nc} is the work done by the nonconservative forces and δ indicates the first order variation. By neglecting the inertial

effects in the longitudinal direction, T_k is given by

$$T_k = \frac{1}{2}\int_o^L \int_{A_T} \rho(\dot{v}_Y^2 + \dot{w}_Z^2) dA ds \; + \frac{1}{2}\sum_{k=1}^{p}[m_{sk}V^2(s_k,t) + m_{sk}W^2(s_k,t) + I_{sk}\Theta^2(s_k,t)] \quad (3.5)$$

where L is the total length of a line in a span; ρ is the mass density of the iced bundle conductors' total cross-sectional area, A_T; m_{sk} and I_{sk} are the mass and the mass moment of inertia of the kth spacer, respectively; s_k is the intrinsic coordinate of the kth spacer's intersection with the reference curve; p is the number of spacers; and a dot superscript indicates differentiation with respect to time, t. The variation of the strain energy for a bundle's bulk motion, δV_s, can be obtained by summing the strain energies of each of its conductors [15, 48], i.e.

$$\delta V_s = \sum_{i=1}^{n}\int_0^L [AE\delta\epsilon_s\epsilon_s + B_T(\delta\epsilon_s\epsilon_\theta + \epsilon_s\delta\epsilon_\theta) + GJ\delta\epsilon_\theta\epsilon_\theta + T\delta\epsilon_s + M_t\delta\epsilon_\theta]_i ds \; . \quad (3.6)$$

Suffix i in equation (3.6) represents the ith conductor again and n is the total number of conductors in a bundle. ϵ_s is the Lagrangian strain of the ith conductor, along s, such that

$$\epsilon_s = \frac{\partial x}{\partial s}\frac{\partial u_X}{\partial s} + \frac{\partial y}{\partial s}\frac{\partial V_i}{\partial s} + \frac{\partial z}{\partial s}\frac{\partial W_i}{\partial s} + \frac{1}{2}[(\frac{\partial u_X}{\partial s})^2 + (\frac{\partial V_i}{\partial s})^2 + (\frac{\partial W_i}{\partial s})^2]. \quad (3.7)$$

On the other hand, the torsional strain of a conductor, ϵ_θ, can be expressed as

$$\epsilon_\theta(s) \;\; = \;\; \frac{\partial\Theta(s)}{\partial s}. \quad (3.8)$$

T in equation (3.6) is the static tension in each conductor, M_t is a conductor's initial internal twisting moment that resists the external moment caused by an eccentric ice weight, A and GJ are the cross sectional area and the torsional rigidity of a bare conductor, respectively, E is the modulus of elasticity and B_T represents an axial-torsional coupling [49].

The variation of the virtual work is described by

$$\delta W_{nc} = \int_0^L [F_y(s)\delta V + F_z(s)\delta W + F_\theta(s)\delta\Theta]ds - \delta\mathbf{q}_a^T\mathbf{C}_a^T\dot{\mathbf{q}}_a \; . \quad (3.9)$$

F_y, F_z and F_θ are the aerodynamic loads (per unit span length of the bundle) which act at the reference curve in the y, z and θ directions, respectively. $\mathbf{C_a}$ is an experimentally found

damping matrix that takes the form

$$\mathbf{C}_a = \begin{bmatrix} 0 & \mathbf{0_3} \\ \mathbf{0_3^T} & \mathbf{C} \end{bmatrix} \tag{3.10}$$

where $\mathbf{0_3}$ is the 1×3 null matrix. On the other hand, the elements of the diagonal matrix $\mathbf{C}$ are

$$c_{11} = 2\omega_y \xi_y m_{11}, \quad c_{22} = 2\omega_z \xi_z m_{22}, \quad c_{33} = 2\omega_\theta \xi_\theta m_{33} \ . \tag{3.11}$$

ω_i ($i = y, z, \theta$) and ξ_i ($i = y, z, \theta$) are, respectively, the bundle's undamped, uncoupled natural frequencies and the measured damping ratios associated with the uncoupled vibrations in the direction indicated by a subscript. m_{ii} ($i = 1, 2, 3$) are the elements of the matrix $\mathbf{M}$ defined in equation (3.14). Finally, $\mathbf{q}_a$ in equation (3.9) is defined by

$$\mathbf{q}_a^T = (q_u \ \mathbf{q}^T) \ where \quad \mathbf{q}^T = (q_v \ q_w \ q_\theta). \tag{3.12}$$

Substituting equations (3.5) through (3.12) into equation (3.4) yields the equations of motion as

$$\mathbf{M}_a \ddot{\mathbf{q}}_a + \mathbf{C}_a \dot{\mathbf{q}}_a + \mathbf{K}_a \mathbf{q}_a = \mathbf{F}_a \tag{3.13}$$

where $\mathbf{M}_a$ and $\mathbf{K}_a$ are a 4×4 mass matrix and stiffness matrix, respectively. $\mathbf{M}_a$ takes the form

$$\mathbf{M}_a = \begin{bmatrix} 0 & \mathbf{0_3} \\ \mathbf{0_3^T} & \mathbf{M} \end{bmatrix} \tag{3.14}$$

and the non-zero elements of $\mathbf{M}$ and $\mathbf{K_a}$ are given more conveniently in the Appendix **A**. The aerodynamic load vector, $\mathbf{F_a}$, in equation (3.13) is found at the reference curve from aerodynamic data measured at the centers of the individual conductors of a bundle. It is represented as

$$\mathbf{F}_a^T = (0 \ \mathbf{F}^T) \ . \tag{3.15}$$

The components of $\mathbf{F}^T = (F_y \ F_z \ F_\theta)$ are expressed conventionally as nonlinear functions of the wind's angle of attack α, the conductor's diameter d, side wind speed U_z, and the density of

air, ρ_{air}. In an analogous fashion to a single conductor, they are approximated in section **A.3** of Appendix **A** as cubic polynomials in α where

$$\alpha = \Theta - \frac{d}{2U_z}\dot{\Theta} - \frac{\dot{V}}{U_z} \tag{3.16}$$

by assuming that

$$\tan^{-1}(\frac{d}{2U_z}\dot{\Theta} + \frac{\dot{V}}{U_z}) \simeq \frac{d}{2U_z}\dot{\Theta} + \frac{\dot{V}}{U_z} \tag{3.17}$$

and approximating the characteristic radius [13] by $d/2$. The major difference for a bundle conductor is that the reference curve is used to define α rather than the single conductor itself. See, for example, Fig.3.2. It is assumed, for simplicity, that the aerodynamic interactions between the different conductors of a bundle are negligible. This assumption appears intuitively more reasonable for wider separations of the conductor. For example, it seems increasingly plausible when the separation between the conductors of a twin bundle is enlarged beyond ten conductor diameters [50]. Then the aerodynamic forces and moments measured for an individual conductor can be merely summed at the reference curve. Details of the basic aerodynamic loads considered here are given in reference [15]. They correspond to the single iced conductor illustrated in Fig.3.1(b).

The equations of motion for the condensed 3DOF system are obtained from equation (3.13) by partitioning $\mathbf{K}_a$ so that

$$\mathbf{K}_a = \begin{bmatrix} k_{11} & \mathbf{K_2} \\ \mathbf{K_2}^T & \mathbf{K_3} \end{bmatrix}. \tag{3.18}$$

By eliminating the terms associated with the axial displacements, equation (3.13) becomes

$$\mathbf{M\ddot{q}} + \mathbf{C\dot{q}} + \mathbf{Kq} = \mathbf{F} \tag{3.19}$$

where

$$\mathbf{K} = \mathbf{K_3} - \mathbf{K_2}^T {k_{11}}^{-1} \mathbf{K_2}. \tag{3.20}$$

3.4 Finite element model

A FE model established in this section not only provides the necessary mode shapes for the

hybrid model but also extends the twin bundle [35] method to a bundle having any number of conductors. Consider, next, a bundle consisting of n conductors. Each conductor is considered to have n_p nodes. The jth nodes of all the conductors are assumed to be connected either by a physical or a ficticious, rigid spacer. In the FE formulation, the relevant mass, stiffness and damping matrices as well as the nodal force vector are formulated for each conductor of the bundle. These equations are transformed to the reference curve with the help of the physical or ficticious rigid spacers.

All but two of the assumptions used to develop the hybrid model are utilized in the FE modelling of a bundle conductor. The exceptions avoid the neglect of the longitudinal inertias and the assumption of solely a single mode acting in a specified direction. Details of the FE formulation have been given previously for a single conductor [51]. As before, a conductor is represented by employing three node, isoparametric cable elements. After forming the equations of motion for each conductor, transforming them to the reference curve and assembling the matrices, the final equations take the form

$$[M]\{\ddot{q}\} + [C]\{\dot{q}\} + [K]\{q\} = \{F\} \tag{3.21}$$

where

$$\begin{aligned}
[M] &= \sum_{i=1}^{n} [T^{(i)}]^T [M^{(i)}][T^{(i)}] \; + \; [M_s] \\
[C] &= \sum_{i=1}^{n} [T^{(i)}]^T [C^{(i)}][T^{(i)}] \\
[K] &= \sum_{i=1}^{n} [T^{(i)}]^T [K^{(i)}][T^{(i)}] \\
\{F\} &= \sum_{i=1}^{n} [T^{(i)}]^T \; \{F^{(i)}\} \\
\{q\} &= \{\{q_1\}^T, \; \{q_2\}^T, \ldots, \{q_{n_p}\}^T\}^T
\end{aligned} \tag{3.22}$$

and

$$\{q_j\}^T = (U_j^{(i)}, V_j^{(i)}, W_j^{(i)}, \Theta_j^{(i)}).$$

$U_j^{(i)}, V_j^{(i)}$ and $W_j^{(i)}$ are the global displacements of node j of the reference curve and $\Theta_j^{(i)}$ is the rotation of the bundle about the reference curve. The $[M^{(i)}]$, $[C^{(i)}]$ and $[K^{(i)}]$, $i = 1, 2, ..., n$, are respectively the mass, damping and stiffness matrices of size $4n_p \times 4n_p$. $\{F^{(i)}\}$ is the corresponding load vector of size $4n_p \times 1$. The construction of these matrices is given in reference [51]. $[T^{(i)}]$ is a 4×4 transformation matrix whose non-zero elements are $T_{11} = T_{22} = T_{33} = T_{44} = 1, T_{24} = r_i \cos\theta_{i0}$, and $T_{34} = r_i \sin\theta_{i0}$. Again, r_i is the distance between the reference curve and the center of the ith bare conductor and θ_{i0} is the initial clockwise angle of this conductor as viewed from the positive direction of the y axis. See Fig.3.1(b). If the Delta function, δ_{sj}, is denoted by

$$\delta_{sj} = \begin{cases} 0 & \text{for a massless, fictitious spacer introduced at node } j \\ 1 & \text{for a physical spacer having an end at node } j \end{cases} \tag{3.23}$$

then the diagonal mass matrix, $[M_s]$, in equation (3.22), which represents the contribution from the physical spacers' inertias, can be written as

$$[M_s] = \begin{bmatrix} \delta_{s1}\, M_{s1} & 0 & & \cdots & 0 \\ 0 & \delta_{s2}\, M_{s2} & 0 & \cdots & 0 \\ \vdots & \ddots & \ddots & \ddots & \vdots \\ 0 & \cdots & 0 & \delta_{s(n_p-1)}\, M_{s(n_p-1)} & 0 \\ 0 & \cdots & & 0 & \delta_{sn_p}\, M_{sn_p} \end{bmatrix}. \tag{3.24}$$

The diagonal matrix $[M_{sj}]$ is given by

$$[M_{sj}] = \begin{bmatrix} m_{sj} & 0 & 0 & 0 \\ 0 & m_{sj} & 0 & 0 \\ 0 & 0 & m_{sj} & 0 \\ 0 & 0 & 0 & I_{sj} \end{bmatrix} \tag{3.25}$$

where m_{sj} and I_{sj} are the mass of the physical spacer and its mass moment of inertia about the reference curve at node j, respectively. Note that the mode shapes, $f_u(s)$, $f_v(s)$, $f_w(s)$ and $f_\theta(s)$ in equation (3.2) are taken in the discretized form as

$$(f_u, f_v, f_w, f_\theta) = (U^i, V^i, W^i, \Theta^i) \tag{3.26}$$

3.5 Stability analysis and limit cycles

Steps involved in the stability analysis of the static configuration and the determination of the limit cycles are detailed in reference [15] for the hybrid model or in reference [34] for the FE model. Hence, only a brief description is given here.

The first step in determining the feasibility of galloping is to investigate whether the initial equilibrium solution (IES) of the linearized form of equation (3.19) or (3.21) is stable. The characteristic polynomial corresponding to equation (3.19) or (3.21) can be obtained by using the same approach in deriving equations (2.12), (2.14) and (2.15). If all the eigenvalues of the the resulting characteristic polynomial have negative real parts, then the static configuration is asymptotically stable and a further analysis is not required. If, however, at least one of the eigenvalues crosses the real axis (a critical point) when a parameter changes, say an increasing wind speed U_z, then the IES becomes unstable and galloping may be initiated. The critical wind speed, U_{zc}, is the value at which the IES just becomes unstable. Once the IES becomes unstable, new equilibrium states or dynamic motions, which are periodic or quasi-periodic, may emerge from the critical point. (Note that chaotic states are not investigated.) Perturbation techniques are employed to study the dynamic motions and to find the limit cycles' amplitudes. The derivation of the limit cycles and their stability conditions was summarized in Chapter 2. Explicit expressions to determine the IES and the limit cycles' amplitudes are given in reference [15] for the hybrid model. On the other hand, a step-by-step procedure is given in reference [34] for computing the dynamic motion using FE model.

3.6 Numerical results

In this section, natural frequencies and limit cycles of the line with ice shape C11 [50] are used to make a comparison between the hybrid model and FE model for different conductor configurations. A trend analysis is important for engineers due to certain key parameters so that numerical results focus on the effects of a bundle's parameters like the horizontal tension

of a conductor, span length, structural damping, critical wind speed and wind speed above critical wind speed.

The examples considered here assume that all conductors in the bundle are identical. Furthermore, the iced conductors have simple end supports which permit longitudinal degrees of freedom so that a more realistic interaction can be accommodated between adjacent spans. Ice accumulations on the conductors, whose asymmetry may causes the conductors' instability, are obtained from a single conductor sample placed in a freezing rain simulator [50]. The resulting (C11) cross–section is illustrated in Figure 3.1(b). It resembles the D form used traditionally to induce galloping in field trials [4]. This particular ice formation is assumed to be accreted identically on each conductor. In other words, variations in the ice shape that could arise from one conductor partially shielding another conductor from the wind are ignored for simplicity. The wind speed is also presumed to be constant along the span.

3.6.1 Natural frequencies and limit cycles

Limit cycle amplitudes, mainly the components in the vertical and horizontal directions, are important in avoiding an electrical flashover or the clashing of conductors. They are related not only to the aerodynamic loads but also to the natural frequencies of the conductors. In particular, natural frequencies determine if an internal resonance happens which, in turn, crucially affects the dynamic behavior of the conductors. An internal resonance occurs when the ratio of at least two of the natural frequencies is close to a ratio of two positive integers. The parameters in Table 3.1 are selected so that the lowest horizontal mode participates in an internal resonance. In this table, I is the centroidal inertial moment of the bare conductor; e_y and e_z represent the eccentricity in the y and z directions, respectively. A_{ice} is a total cross sectional area of the iced conductor and m is the corresponding mass per unit length. Table 3.2 gives a comparison of the lowest three natural frequencies of various bundles and a single conductor in plunge (vertical), swingback (horizontal) and torsion that are predicted by the hybrid and FE models. The finite element model has 21 nodes along the reference curve where

numbers 1 and 21 represent the left and right supports, respectively, and 19 fictitious spacers are always used for all bundle configurations.

Table 3.2 indicates that the percentage differences between the natural frequencies produced by the hybrid and FE models are within an acceptable 1%, The natural frequencies corresponding to a plunge (vertical) or swingback (horizontal) motion are almost the same for a given number of loops per span, regardless of the number of conductors. This behavior occurs because the mass and stiffness in these directions change almost identically with an increasing number of conductors. The torsional frequencies, on the other hand, decrease noticeably as more conductors are added because the change in the moment of inertia is greater than that for the stiffness. Identical trends have also been observed from existing bundle models [5, 30].

The hybrid and finite element models are employed to investigate the dynamic limit cycle amplitudes. From a practical viewpoint, one through three loops per span are usually considered in North America because they are most frequent for galloping [2]. The examples in this paper, however, only give the mid-span and quarter span results for one and two loops per span galloping, respectively, because the limit cycle amplitudes for the three loops per span case are invariably much smaller. The initial placements of the different bundle configurations are shown in Fig.3.2. The corresponding aerodynamic coefficients, a_{ij}, are given in Table 3.3 for $\theta_{static} = 40^0$ and $\theta_{static} = 270^0$. Only data for single conductor is shown in Table 3.3 because the bundle conductors are invariably stable when $\theta_{static} = 270^0$. Both the hybrid and finite element models predict that, regardless of the number of conductors in a bundle, the initial equilibrium state is unstable at the assumed 4m/s wind speed (i.e. the stability criterion is first violated [15]). A 1:1:0 ($\omega_y : \omega_z : \omega_\theta$) resonant galloping occurs in a one loop per span motion for the single as well as for the bundle conductors. In addition, a 1:1:1 resonant galloping can occur but only for a two loops per span motion of the bundle conductors. Figs.3.3(a) and (b) compare the resulting bulk motion limit cycles for one and two loops per span motions, respectively. The results from the hybrid model agree with the FE predictions. The A_y and A_z used in this figure correspond to the vertical and horizontal limit cycle amplitudes for the

single conductor or the reference curve of a bundle. It can been seen from Fig.3.3(a) that the vertical amplitudes for the one loop per span case are invariably comparable in magnitude. They are much greater than the horizontal displacements for the bundle conductors so that the plunge motion dominates the one loop per span galloping for the bundles. Therefore, it is not surprising that a predominantly vertical conductor motion has a high percentage of occurrence in the field [2]. On the other hand, Fig.3.3(b) suggests that the horizontal motion is comparable or larger in magnitude to that of the plunge for a two loops per span oscillation. Therefore, the horizontal motion should not be neglected in such cases.

3.6.2 Critical and higher wind speed trends

Two static angles of attack, $\theta_{static} = 40^0$ or 270^0, are selected to illustrate that the classical Den Hartog criterion, which depends only upon the aerodynamic characteristics of the conductors, does not necessarily give the initiation of galloping. According to this criterion, an instability occurs when $\frac{\partial C_L}{\partial \alpha} + C_D < 0$. C_L and C_D are purely the aerodynamic lift and drag coefficients, respectively, which are defined in the Appendix **A**. The previously considered single and bundle conductors are used again to determine how the ensuring dynamic limit cycle amplitude changes with the critical wind speed and an increasing steady side wind speed beyond this critical value.

Figure 3.4 shows the variation in the reduced critical wind speed, $\bar{U}_{zc} = U_{zc}/fL_x$, and the nondimensional limit cycle amplitude, $\bar{A} = \sqrt{A_y^2 + A_z^2}/s_a$, at the static angle of attack $\theta_{static} = 40^0$. (Note that this particular angle is illustrated in both Figs.3.1(b) and 3.2.) The f is taken as the lowest ω_y, the predominantly vertical natural frequency; L_x is the horizontal span length; and s_a is the static sag at a line's mid-span. The figure indicates that $\bar{A}$ invariably decreases as $\bar{U}_{zc}$ increases, immaterial of the number of loops per span and regardless of the number of conductors in a bundle. However, the single conductor always has the lowest $\bar{A}$ at a given $\bar{U}_{zc}$. On the other hand, the vertical amplitude, A_y, always dominates $\bar{A}$ in Fig.3.4(a) while A_z is the principal component of $\bar{A}$ in Fig.3.4(b). Fig.3.5 presents analogous results to

Fig.3.4(a) for $\theta_{static} = 270^0$. Only data for the single conductor is shown in Fig.3.5 because the bundle conductors are invariably stable when $\theta_{static} = 270^0$. The major difference from Fig.3.4(a) is that the Den Hartog criterion is satisfied no longer for the single conductor. (Table 3 indicates that $\frac{\partial C_L}{\partial \alpha} + C_D$ is negative at $\theta_{static} = 40^0$ but positive at $\theta_{static} = 270^0$.) Despite this difference, the single conductor remains unstable - otherwise there would be no limit cycle amplitudes in Fig.3.5! Clearly, the simple Den Hartog criterion is not always applicable. On the other hand, $\bar{A}$ decreases again with increasing $\bar{U}_{zc}$, albeit more rapidly at the lowest $\bar{U}_{zc}$.

Figs.3.6 and 3.7 give the changes in the component nondimensional limit cycle amplitudes, $\bar{A}_y$ and $\bar{A}_z$, as the steady wind speed rises above the reduced critical wind speed, $\bar{U}_{zc}$, for $\theta_{static} = 270^0$ and 40^0, respectively. In these figures, the static horizontal tension is H=30kN, the span length is $L_x = 126m$ while $\bar{U}_z = U_z/fL_x$, $\bar{A}_y = A_y/s_a$ and $\bar{A}_z = A_z/s_a$. The wind speed, U_z, varies from a steady 4 m/s to a steady 6 m/s. Not surprisingly, both $\bar{A}_y$ and $\bar{A}_z$ always grow as $\bar{U}_z$ and, hence, the wind's energy input to a line increases. As before, $\bar{A}_y$ is invariably much larger than $\bar{A}_z$ for one loop per span galloping but this trend is usually reversed for two loops per span. The single conductor is the exception in the latter situation because the internal resonance and, hence, the coupling between the torsional and vertical or horizontal movements does not change. On the other hand, when galloping occurs, the number of conductors in a bundle hardly affects $\bar{A}_y$ and $\bar{A}_z$.

3.6.3 Trends for static horizontal tension and span length

The effects on $\bar{A}_y$ and $\bar{A}_z$ of increasing the nondimensional static horizontal tension, $\bar{H} = H/w$, and span length, L_x/s_a, are given in Figs.3.8 and 3.9, respectively, for $\theta_{static} = 40^0$. Here w is the total weight of a bare conductor in one span. Both $\bar{A}_y$ and $\bar{A}_z$ invariably tend to grow as either $\bar{H}$ or L_x/s_a increases. The single loop per span case (Figs.3.8(a) and 3.9(a)) is little different to the comparable situation observed in Fig.3.7(a) for increasing $\bar{U}_z$. However, unlike before, the twin bundle has somewhat smaller $\bar{A}_y$ and $\bar{A}_z$ than the triple and quad bundles in two loops per span galloping, especially for enlarged $\bar{H}$. This difference is likely caused by

the different torsional coupling to these components that arise from the appreciably smaller rotation of the twin bundle at higher $\bar{H}$.

3.7 Concluding remarks

A flexible and computationally efficient design tool is developed for bundle conductors. It can still be used for a single conductor. Software based on this model can be run instantaneously on a personal computer so that it makes a practically required parametric analysis possible. In addition, numerical results for a particular ice shape suggest that the ratio of the limit cycle amplitude to the mid-span's static sag invariably decreases as the critical wind speed ratio increases, regardless of the number of loops per span considered or the number of conductors in a bundle. It also usually grows as the nondimensional side wind speed (above the critical value), horizontal tension or span length increase - again, immaterial of the number of conductors. Den Hartog's criterion for the initiation of galloping is shown to be overly simplified.

Table 3.1 Iced C11 line properties

Parameter	Data	Parameter	Data
d (m)	0.0286	A (mm^2)	423.24
E (N/m^2)	$4.78033*10^{10}$	m (kg/m)	2.379
GJ (Nm^2/rad)	101	ξ_y, ξ_z	$0.515*10^{-3}$
I (kg m)	$0.3334*10^{-3}$	ξ_θ	0.308
H (N)	30000	r_i (m)	0.2355
e_y (mm)	2.05	L_x (m)	125.88
e_z (mm)	-0.63	ρ_{air} (kg/m^3)	1.2929
A_{ice} (mm^2)	594.48	U_z (m/s)	4.0

Table 3.2 Comparison of natural frequencies (Lx=126m, H=30kN)

Number of conductors	No. of loops/span	1			2			3		
	Natural frequencies (Hz)	ω_y	ω_z	ω_θ	ω_y	ω_z	ω_θ	ω_y	ω_z	ω_θ
1	HM	0.482	0.445	1.091	0.891	0.892	4.003	1.337	1.339	6.384
	FM	0.482	0.444	1.090	0.891	0.891	4.003	1.339	1.337	6.385
2	HM	0.482	0.443	0.635	0.892	0.893	1.174	1.341	1.347	1.737
	FM	0.482	0.446	0.635	0.892	0.892	1.174	1.340	1.339	1.737
3	HM	0.482	0.443	0.555	0.892	0.893	1.062	1.341	1.347	1.581
	FM	0.481	0.446	0.555	0.891	0.892	1.062	1.340	1.338	1.581
4	HM	0.481	0.443	0.553	0.892	0.893	1.060	1.341	1.347	1.578
	FM	0.481	0.446	0.553	0.891	0.892	1.060	1.340	1.338	1.578

HM---hybrid model FM---finite element model

Table 3.3 Aerodynamic coefficients for C11

Number of conductors in bundle		Coefficients at $\alpha = 0^o$ and $\theta_{static} = 40^o$		
	i	a_{yi}	a_{zi}	$a_{\theta i}$
Single conductor	1	-0.1667	0.8605	-0.7272
	2	-4.0547	0.8325	0.2935
	3	8.3581	1.7815	5.9704
2	1	-0.3335	1.7210	-1.4543
	2	-8.1094	1.6650	0.5869
	3	16.7162	3.5631	11.9408
3	1	-0.5003	2.5815	-2.1815
	2	-12.1614	2.4975	0.8804
	3	25.0743	5.3447	17.9112
4	1	-0.6670	3.4420	-2.9086
	2	-16.2188	3.3300	1.1738
	3	33.4324	7.1262	23.8816
Single conductor		Coefficients at $\theta_{static} = 270^o$		
	1	0.9423	1.3186	-0.8567
	2	-0.9245	-3.2000	0.9026
	3	2.6352	-13.0623	-0.2353

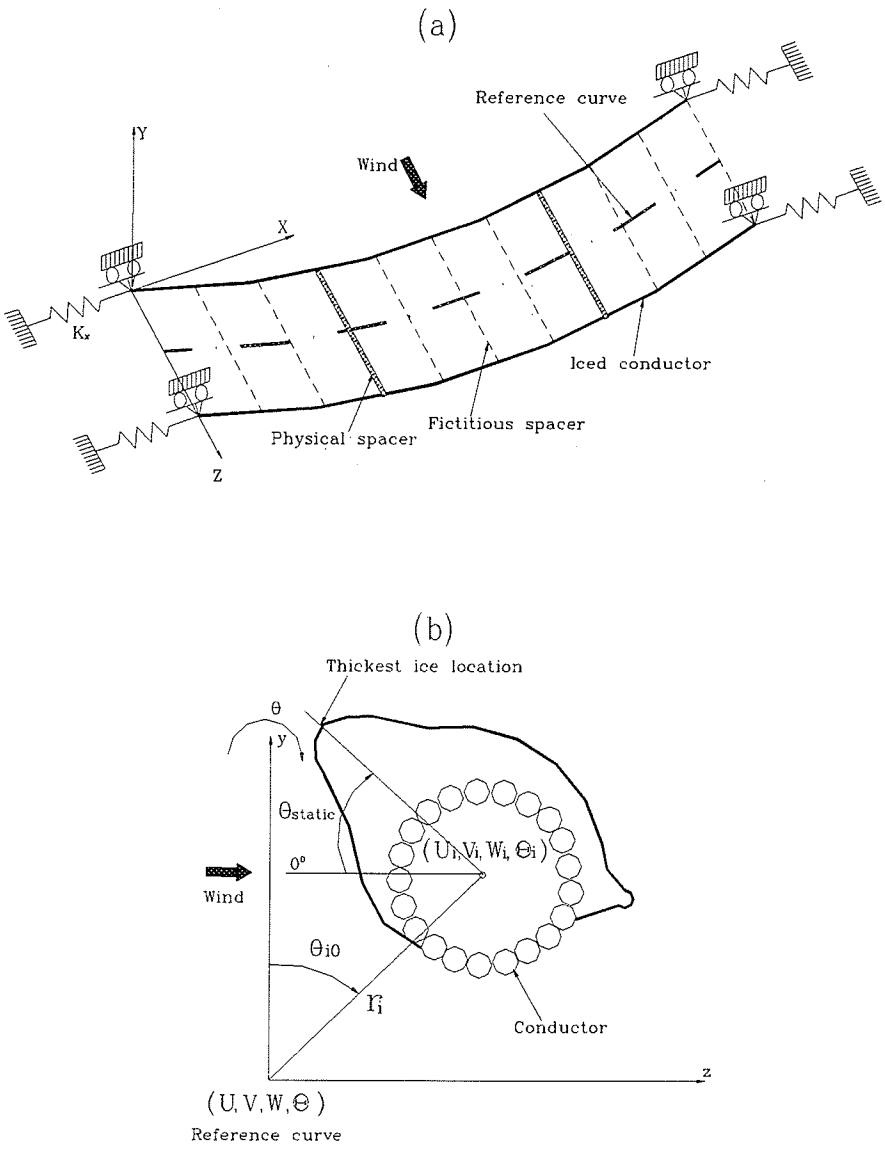

Figure 3.1. Showing (a) the bulk modelling of a twin bundle conductor, and (b) the cross section of the ith iced conductor.

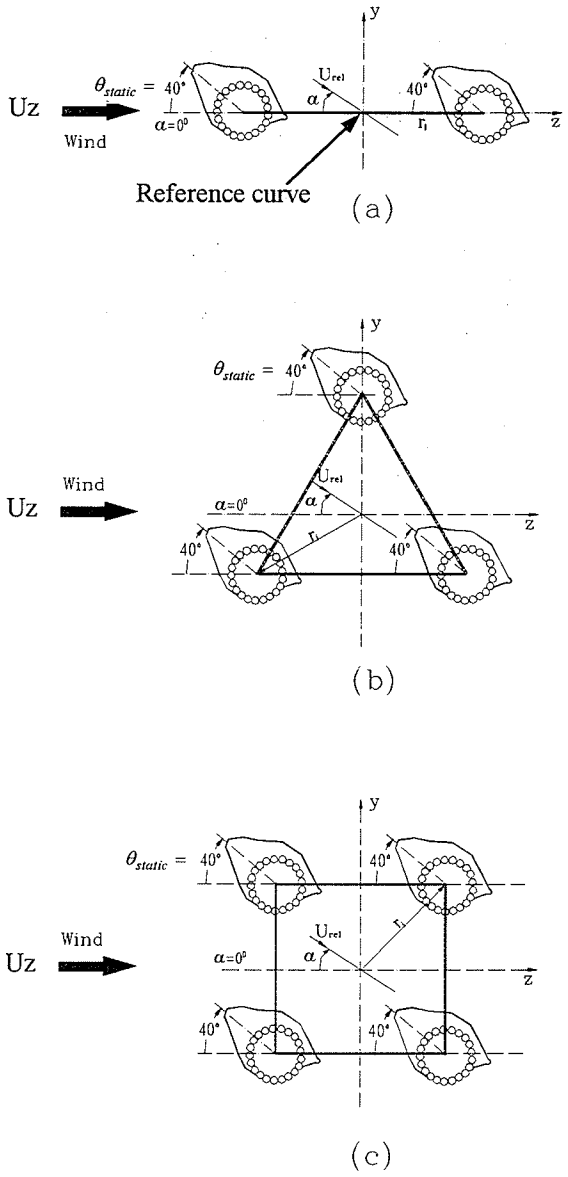

Figure 3.2. The initial arrangement of iced C11 conductors in (a) a twin bundle, (b) triple bundle and (c) quad bundle configuration.

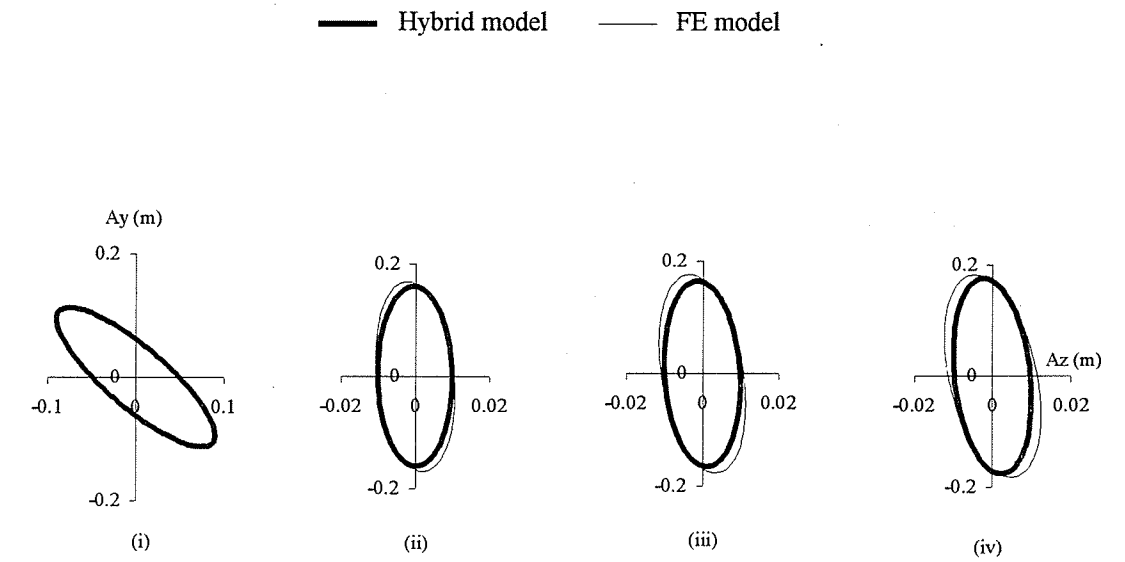

(a)

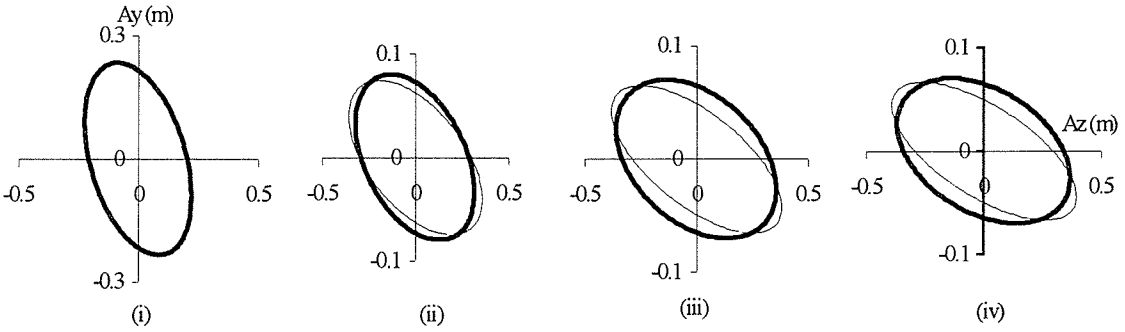

(b)

Figure 3.3 Limit cycle obtained at (a) the mid-span (1 loop/span) and (b) quarter-span (2 loops/span) for (i) a single conductor, (ii) twin bundle, (iii) triple bundle, and (iv) a quad bundle. (Span length Lx=125.88m, horizontal static tension H=30 kN, side wind speed Uz=4m/s, $\alpha = 0^0$ and $\theta_{static} = 40^0$.)

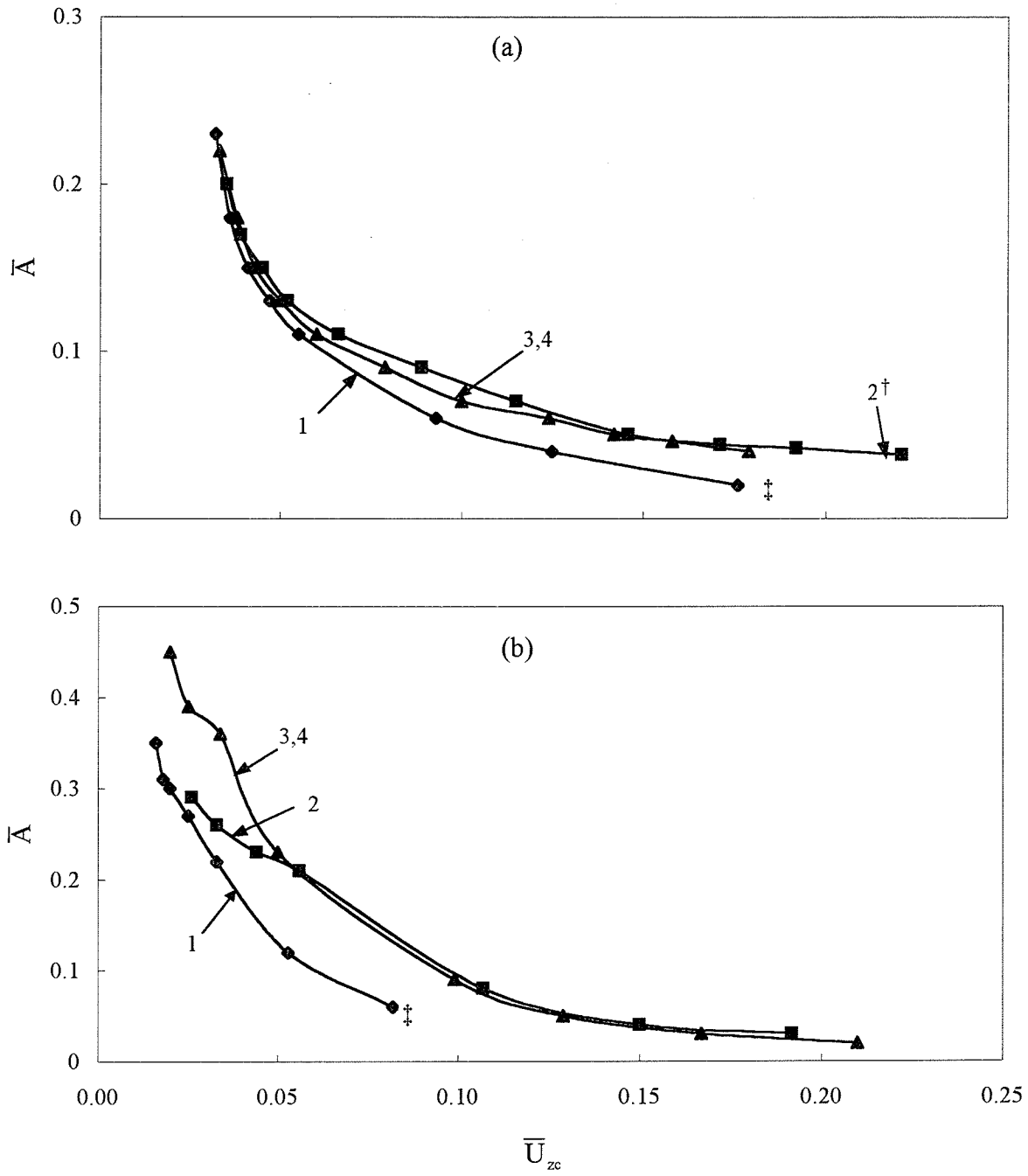

Figure 3.4. Limit cycle amplitude ratio, $\overline{A}$, at different critical wind speed ratios, $\overline{U}_{zc}$, for (a) 1 loop/span and (b) 2 loops/span galloping ($\theta_{static} = 40^0$, $\alpha = 0^0$).
† Number of conductors (in a bundle). ‡ Stable at higher values of $\overline{U}_{zc}$.

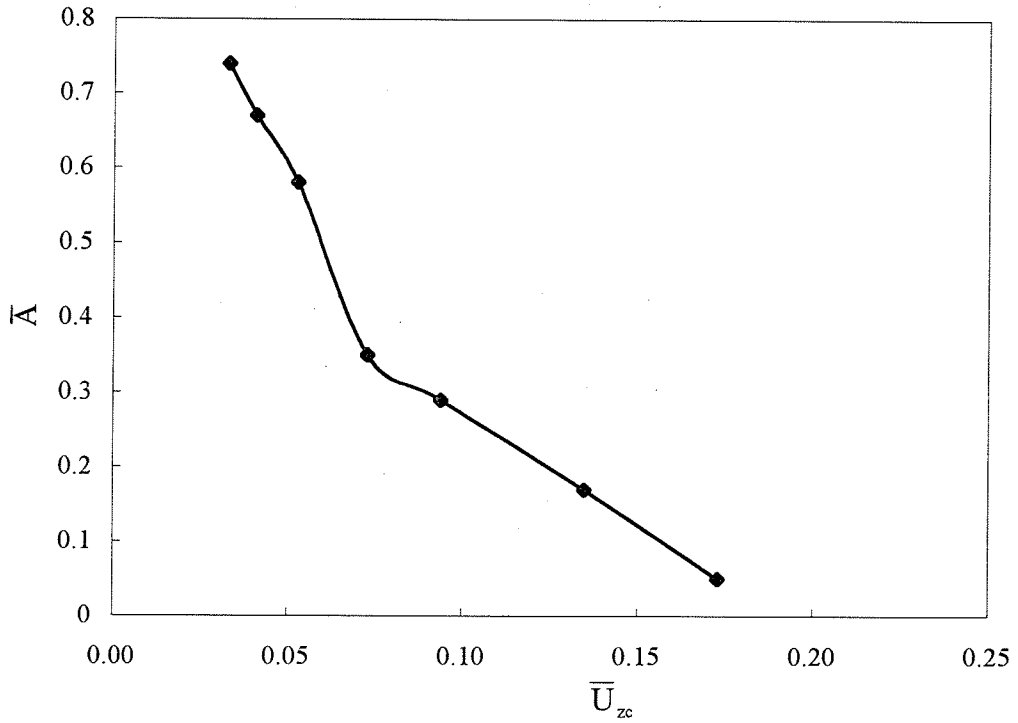

Figure 3.5. Limit cycle amplitude ratio, $\overline{A}$, at different critical wind speed ratios, $\overline{U}_{zc}$, for 1 loop/span galloping of the single conductor. ($\theta_{static}=270^0$)

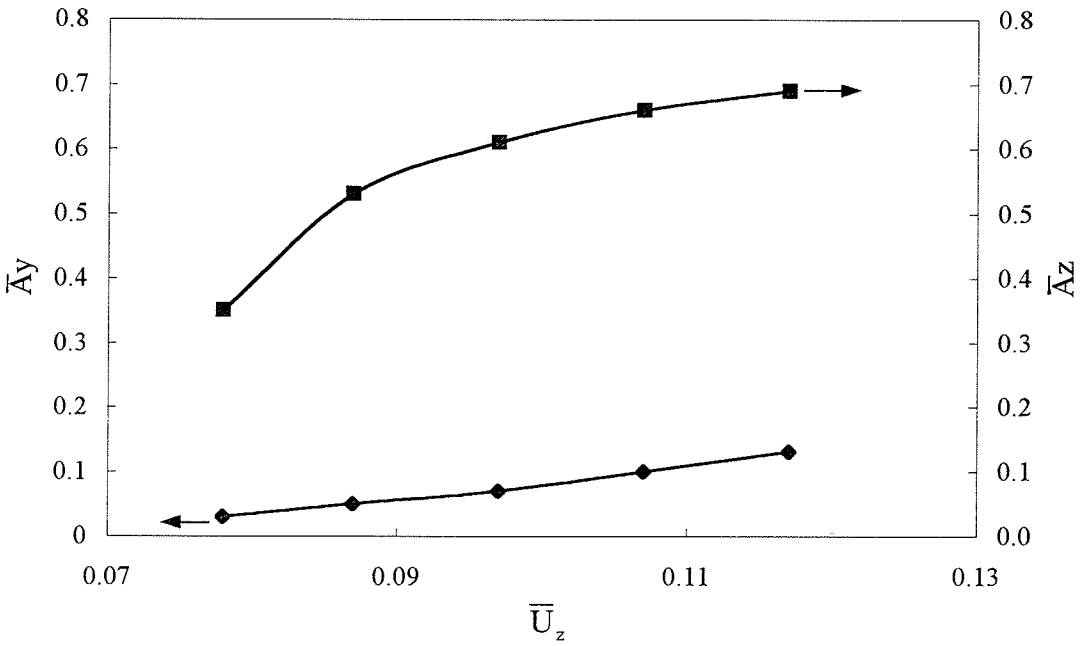

Figure 3.6. Limit cycle amplitude ratios, $\overline{A}_y$ and $\overline{A}_z$, at different wind speed ratios, $\overline{U}_z$, for 1 loop/span galloping of the single conductor. ($\theta_{static}=270^0$).

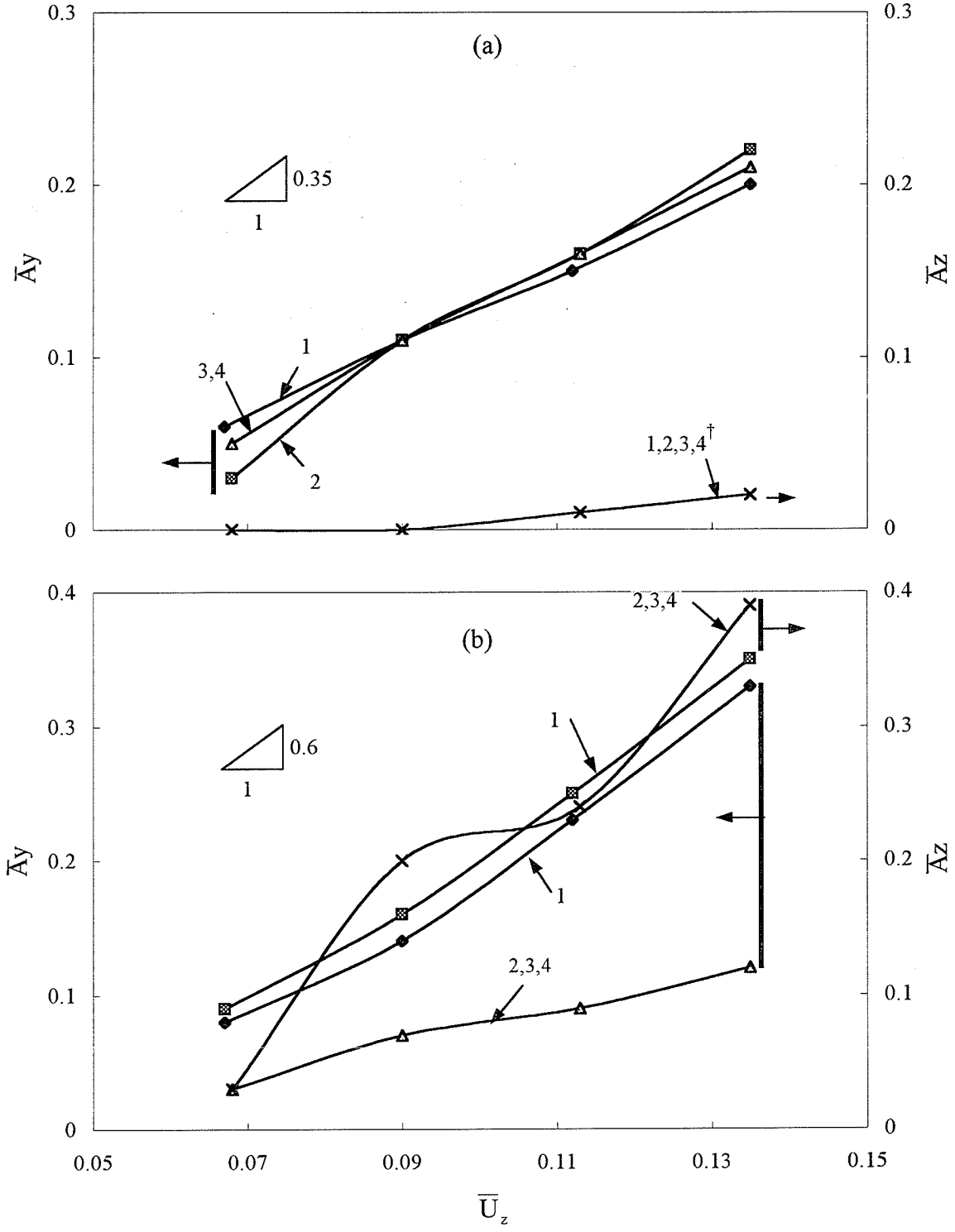

Figure 3.7. Limit cycle amplitude ratios, $\overline{A}_y$ and $\overline{A}_z$, at different wind speed ratios, $\overline{U}_z$, for (a) 1 loop/span galloping and (b) 2 loops/span galloping.
† Notation as in Figure 3.4. ($\alpha = 0$, $\theta_{static} = 40^0$)

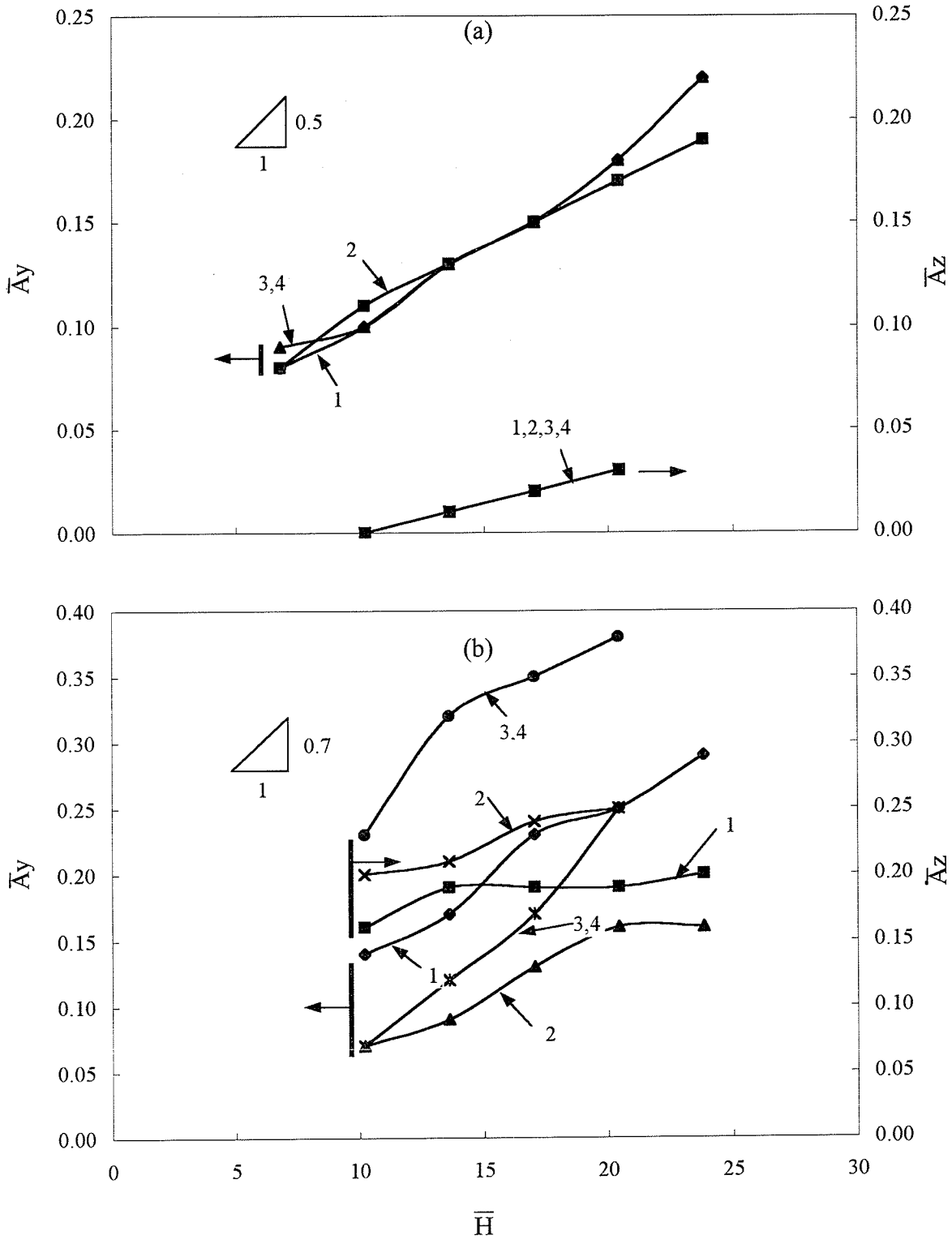

Figure 3.8. Limit cycle amplitude ratios, $\overline{A}_y$ and $\overline{A}_z$, at various horizontal tension ratios, $\overline{H}$, for (a) 1 loop/span galloping (b) 2 loops/span galloping. Horizontal span length, Lx, is invariably 126m. ($\alpha = 0$, $\theta_{static} = 40^0$)

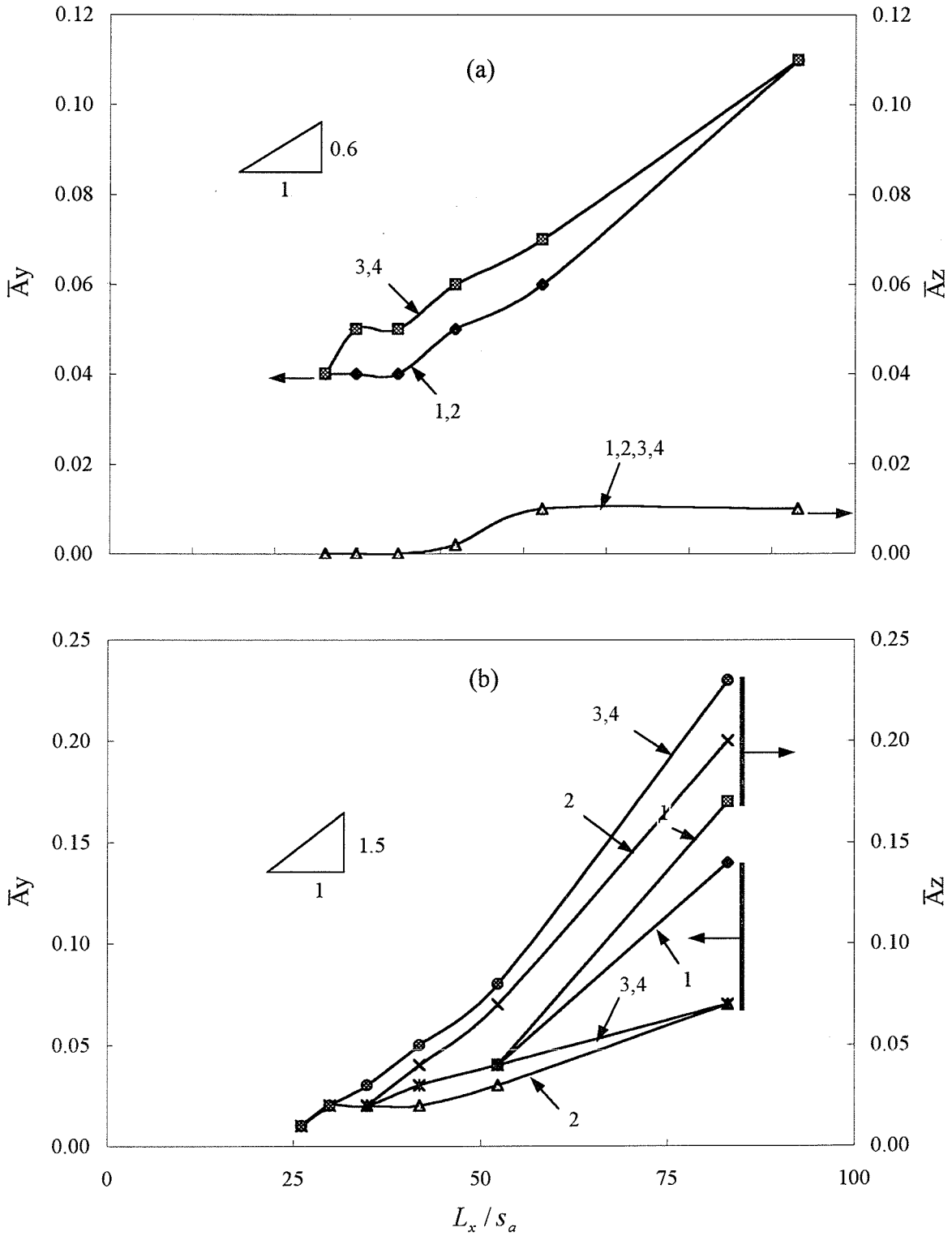

Figure 3.9. Limit cycle amplitude ratios, $\overline{A}_y$ and $\overline{A}_z$, at various span length ratios, L_x / s_a, for (a) 1 loop/span galloping (b) 2 loops/span galloping. Horizontal static tension, H, is always 30kN. ($\alpha = 0$, $\theta_{static} = 40^0$)

Chapter 4

GALLOPING CONTROL: HYBRID DAMPER

4.1 Introduction

As introduced in Section 1.2.3, there is no control device that is suitable for all atmospheric conditions or all kinds of galloping. A detuning pendulum is the most popular control device used in North America. It can adjust the torsional frequencies of a conductor to avoid the strong coupling between the vertical and torsional movements. However, the detuning pendulum makes no contribution to the structural damping which is very important to alleviate galloping. Several transmission lines have been observed to still undergo galloping, in some circumstances, even though detuning pendulums have been installed on them. Thus, it is difficult to develop a control device that can prevent galloping for all conditions. One reason is that the galloping mechanisms are not understood completely. However, it is always beneficial if the structural damping of a line can be increased by adding a control device. Indeed, it could be cost effective to increase an existing transmission line's structural damping by adding a passive device so that the height of towers and conductor clearances could be reduced. A hybrid damper (HD) has potential in this area. A HD consists of a rigid link, spring and a liquid damper, as shown in Fig.4.1. The end of the rigid link is fixed at a conductor and the other is hinged at a container containing the liquid. The natural rotational frequency of the HD can be tuned by the equivalent twist spring. Therefore, the conductor's motion is partially converted to a rotation of the liquid container so that the liquid sloshes back and forth between the container's ends to provide structural damping. The liquid container is modelled by a large weight for a detuning pendulum. In this chapter, the previous computer software has been modified to accommodate HDs and, thus, test their effectiveness in alleviating galloping. The hybrid model is still used

to describe the motion of a transmission line with simplified HDs. All the assumptions used previously for this the model are also applied here.

The equations of motion for the transmission line with HDs, as well as a parametric analysis of involving HDs are given in the following sections.

4.2 Equations of motion

A HD is mounted so that it is perpendicular to a conductor. Let n_m and β_i be the number of hybrid dampers and the rotation of the ith hybrid damper about its pivot point, respectively. (See Fig.4.1.) β_i can be expressed as

$$\beta_i = \beta_{v_i} q_v + \beta_{w_i} q_w + \beta_{\theta_i} q_\theta \tag{4.1}$$

if only one mode shape is retained for each global variable V, W and Θ. In equation (4.1), β_{v_i}, β_{w_i} and β_{θ_i} are the ith HD's modes corresponding to the y, z and θ directions, respectively. q_v, q_w and q_θ have been defined in equation (3.2). The total kinetic energy, T_d, of all n_m hybrid dampers is

$$T_d = \frac{1}{2}\sum_{i=1}^{n_m}\{m_{d_i}[f_v^2(s_i)\dot{q}_v^2 + f_w^2(s_i)\dot{q}_w^2 + R_{d_i}^2 f_\theta^2(s_i)\dot{q}_\theta^2 - 2R_{d_i} f_w(s_i) f_\theta(s_i)\dot{q}_w\dot{q}_\theta - 2r_{c_i} f_v(s_i)\beta_i\dot{q}_v] + I_{o_i}\beta_i^2\}, \tag{4.2}$$

where m_{d_i}, R_{d_i}, r_{c_i} and I_{o_i} are the ith HD's mass, radius of gyration, the distance between its mass center and pivot point and the moment of mass inertia about the pivot point, respectively. s_i is the ith HD's natural coordinate. f_v, f_w and f_θ have been used in equation (3.2). The variation in the potential energy of the hybrid dampers, δV_d, is given by

$$\delta V_d = \sum_{i=1}^{n_m}\{m_{d_i} g R_{d_i} f_\theta(s_i) q_\theta + k_{\beta_i}\beta_i\delta\beta_i\}, \tag{4.3}$$

where k_{β_i} is the equivalent torsional spring constant of the ith hybrid damper and the g is the gravitational constant. If the linear viscous damping is assumed ($F_{d_i} \propto \dot{\beta}_i$ where F_{d_i} is the damping force of the ith HD), the variation corresponding to the work done by the damping

forces of the HDs is

$$\delta W_d = \sum_{i=1}^{n_m} c_{\beta_i} \dot{\beta}_i \delta \beta_i \tag{4.4}$$

where c_{β_i} is the damping coefficient of the ith hybrid damper. The overall equations of motion that include the HDs can be obtained by inserting equations (4.1) through (4.4) into the corresponding equations (3.5), (3.6) and (3.9) used in the hybrid model without any control device. Then

$$\mathbf{M}'_a \ddot{\mathbf{q}}_a + \mathbf{C}'_a \dot{\mathbf{q}}_a + \mathbf{K}'_a \mathbf{q}_a = \mathbf{F}_a \tag{4.5}$$

where

$$\mathbf{M}'_a = \begin{bmatrix} 0 & \mathbf{0_3} \\ \mathbf{0_3^T} & \mathbf{M} + \mathbf{M}_d \end{bmatrix}, \quad \mathbf{C}'_a = \begin{bmatrix} 0 & \mathbf{0_3} \\ \mathbf{0_3^T} & \mathbf{C} + \mathbf{C}_d \end{bmatrix} \tag{4.6}$$

and

$$\mathbf{K}'_a = \mathbf{K}_a + \begin{bmatrix} 0 & \mathbf{0_3} \\ \mathbf{0_3^T} & \mathbf{K}_d \end{bmatrix}. \tag{4.7}$$

$\mathbf{M}, \mathbf{C}$ and $\mathbf{K}_a$ are the same as the matrices used in equations (3.14), (3.10) and (3.18), respectively. $\mathbf{q}_a$ is defined in equation (3.12). $\mathbf{0_3}$ is still the 1×3 null matrix. $\mathbf{M}_d, \mathbf{C}_d$ and $\mathbf{K}_d$ are contributions from the hybrid dampers. Details are given more conveniently in Appendix B.

4.3 Numerical results

Results from parametric analyses of hybrid dampers are given in this section. Two main parameters of a HD are selected to test their effect on galloping. One is the damper's natural undamped frequency, ω_d, and the other is its damping ratio, ξ_d. Here $\omega_d = \sqrt{k_\beta / I_o}$ and $\xi_d = c_\beta / 2 m_d \omega_d$. The corresponding results for a completely untreated line and one having detuning pendulums (DP), i.e. a "reference" control device which has been used for many years, are given for comparison. The examples are given for a single conductor and for one or two loop motions per span. The line's unexplained physical parameters and the aerodynamic coefficients for C11 are listed in Tables 3.1 and 3.3. Parameters for the DP are selected according

to Ontario Hydro's guidelines [54]. The weight and radius of gyration of DP used here are $11kg$ and $0.145m$, respectively.

4.3.1 Effects of HD's natural frequency

In Figs.4.2 and 4.3, λ represents the ratio of the conductor's natural frequency in plunge to the HD's natural frequency, i.e. $\lambda = \omega_y/\omega_d$. $\bar{A}_y$ and $\bar{A}_z$, which were defined in section 3.6.2, are the non-dimensional limit cycle amplitudes in the vertical and horizontal directions, respectively. $\bar{U}_{zc}$ is the non-dimensional critical wind speed which was defined in section 3.6.2. Fig.4.2 corresponds to a line with one HD located at its mid-span. The line undergoes one loop per span galloping before the HD is added. This figure gives the non-dimensional critical wind speed and limit cycle amplitude for different λ and ξ_d. It can be seen that, when $\lambda = 1$ (i.e. the HD's natural frequency equals the lowest natural frequency of the line in the vertical direction), the critical wind speed increases most noticeably and the ensuing limit cycle amplitude decreases, especially at a larger ξ_d. Indeed, the greater rotation of the HD when $\lambda = 1$ leads to larger damping due to a larger β_{v_k} in equation (B.9). Moreover, the different slopes of these curves, which correspond to different λ, illustrate the effectiveness of the HD's damping. On the other hand, Tables 4.1 and 4.2 as well as Fig.4.2 indicate that the detuning effects of a DP or a HD are not significant when $\xi_d = 0$ compared to the untreated line. (Actually, a hybrid damper corresponds to a conventional DP when $\xi_d = 0$.) The two loops/span galloping case is not given because the HD or DP is located exactly at mid-span, i.e. at the node of the second mode, so that they are both ineffective.

Fig.4.3 shows one or two loops per span galloping for a line with 3 HDs which are located at $\frac{1}{4}L_x$, $\frac{5}{12}L_x$ and $\frac{2}{3}L_x$, respectively. This HD arrangement is consistent with Ontario Hydro's guidelines about a DP arrangement. The natural frequency of the HD near the line's mid-span is adjusted to be equal to the lowest natural frequency of the conductor in plunge (without any HDs). The natural frequencies of the two remaining HDs, however, are tuned to this conductor's second natural plunge frequency. This approach is to alleviate galloping that

corresponds to either a one- or two-loop per span situation. Then the damping effect of a given HD intuitively grows as the HD's rotation increases for a given frequency and amplitude of the conductor's motion. Tables 4.1 and 4.3 as well as Figs.4.3(a) and (b) show that the HDs have almost the same effect as the DPs at $\xi_d = 0$ for one loop per span galloping. However, the solution corresponding to the asymmetrical mode is very sensitive to the non-symmetrical arrangement, as shown in Fig.4.3(c) and (d) as well as Table 4.4. The line with HDs raises the limit cycle amplitudes, compared with the untreated or treated line with DPs, except for $\bar{A}_z$ when $\lambda = 0.9$ or 1.1. Table 4.4 indicates that the torsional coupling is involved much more when $\lambda = 1$ for two loops per span galloping. This greater coupling leads to a change in the phase differences between the line's movements in the three directions so that the ratio of the limit cycle amplitudes in the vertical and horizontal directions may be changed significantly. Therefore, galloping in the asymmetrical mode is sensitive to the HDs' arrangement and the selection of their natural frequencies.

4.3.2 Effects of HD's damping ratio

Fig.4.2 presents the non-dimensional critical wind speed and limit cycle amplitude for different damping ratios of a HD. It is seen that the convergence rate of stability is fastest when $\lambda = 1$. The line becomes stable when $\xi_d > 0.7\%(\lambda = 1)$ and $\xi_d > 1\%(\lambda = 1.1)$. On the other hand, the curve for $\lambda = 0.9$ is so flat that the conductor is still unstable when ξ_d is increased to 4%. (Also see Table 4.2.) This behavior occurs because the dissipation of energy is not so efficient when the rotation of the HD is very small for $\lambda \neq 1$. A similar situation appears in Fig.4.3 in which one loop per span galloping occurs in the vertical direction. The convergence rates for all curves presented in Figs.4.3(a) and (b) are slower than those in Fig.4.2 despite three HDs. This is not surprising because two hybrid dampers which are far from a line's mid-span have natural frequencies not tuned to the lowest natural frequency of the conductor. The remaining HD is not located at the point that has maximum displacement even though its frequency is equal to the lowest natural frequency of the line. Thus, these three HDs cannot contribute

larger damping to the system due to a smaller β_{v_k} in equation (B.9). Figs.4.3(c) and (d) give the results for two loops per span galloping. The curve for $\bar{A}_z$ corresponding to $\lambda = 1.0$ is the steepest and the conductor tends to be stable at $\xi_d = 2\%$, although the limit cycle amplitude is larger at $\xi_d = 0$. Moreover, the system becomes stable at $\xi_d = 3\%$ for $\lambda = 0.9$, which does not happen in Figs.4.2, 4.3(a) or (b). The reason is that two off-center, hybrid dampers play a role while only one does in Figs.4.2, 4.3(a) or (b) so that the energy input into the system is dissipated more efficiently.

4.4 Concluding remarks

A model with hybrid dampers (HDs) is developed to assess their effectiveness. A hybrid damper's rotational frequency should be adjusted to correspond to a conductor's lowest natural frequency in either one loop or two loops per span plunge. Furthermore, the selection of the location of the HD depends upon the galloping mode to be alleviated. The numerical examples show that HDs with a 3% to 4% damping ratio can effectively alleviate galloping or even make it become stable. Moreover, HDs display their greater potential for controlling galloping compared with DPs. The hybrid model can be used to optimize the design of a HD and provide guidelines for its application on a transmission line. In future, parametric studies should be conducted to optimize the number, location and parameters of HDs to alleviate galloping.

Table 4.1. Results for the untreated line and the line having one or three detuning pendulums

Span length L_x : 200m
Mass of each pendulum: 11kg
Location of one pendulum: L_x /2
Locations of three pendulums: L_x /4, 5L_x /12, 2L_x /3

Horizontal Tension H: 30kN
Wind speed U_z: 9m/s
$\alpha_{static} = 40^0$

One loop per span	Untreated	Detuning Pendulum	
		One Pendulum	Three Pendulum
Critical wind speed (m/s)	2.647	2.160	2.753
A_y (m)	0.621	0.564	0.779
A_z (m)	0.069	0.087	0.082
A_θ (deg.)	6.203	4.770	1.896

Two loops per span	Untreated	Detuning Pendulum	
		One Pendulum	Three Pendulum
Critical wind speed (m/s)	2.294	2.224	3.372
A_y (m)	0.016	0.010	0.024
A_z (m)	0.225	0.107	0.253
A_θ (deg.)	7.836	7.242	9.058

Table 4.2 Results for the line having one hybrid damper

$\xi = 0$, 0.006, 0.01, 0.02, and 0.04

Span length L_x : 200m
Mass of hybrid damper: 5kg
Location of hybrid damper: $L_x/2$

Horizontal Tension H: 30kN
Wind speed U_z: 9m/s
$\alpha_{static} = 40^0$

One loop per span	ξ	Values of the frequency ratio $\omega_y / \omega_{\theta d}$		
		0.90	1.00	1.10
Critical wind speed (m/s)	0.000	2.161	2.183	2.158
	0.006	2.350	4.742	2.732
	0.010	2.485	Stable	3.227
	0.020	2.860	Stable	Stable
	0.040	3.826	Stable	Stable
A_y (m)	0.000	0.500	0.525	0.504
	0.006	0.490	0.370	0.469
	0.010	0.482	Stable	0.440
	0.020	0.462	Stable	Stable
	0.040	0.410	Stable	Stable
A_z (m)	0.000	0.075	0.085	0.083
	0.006	0.072	0.042	0.072
	0.010	0.069	Stable	0.063
	0.020	0.063	Stable	Stable
	0.040	0.049	Stable	Stable
A_θ (deg.)	0.000	7.055	7.027	7.021
	0.006	6.817	3.835	6.274
	0.010	6.647	Stable	5.634
	0.020	6.169	Stable	Stable
	0.040	4.959	Stable	Stable

Table 4.3 Results for the line having three hybrid dampers and undergoing one loop per span galloping

$\xi = 0$, 0.006, 0.01, 0.02 and 0.04

Span length L_x : 200m
Mass of each hybrid damper: 5kg
Locations of hybrid dampers: $L_x/4$, $5L_x/12$, $2L_x/3$

Horizontal Tension H: 30kN
Wind speed U_z: 9m/s
$\alpha_{static} = 40^0$

One loop per span	ξ	Values of the frequency ratio $\omega_y / \omega_{\theta d}$		
		0.90	1.00	1.10
Critical wind speed (m/s)	0.000	2.748	2.758	2.743
	0.006	2.897	3.837	3.438
	0.010	2.997	4.420	3.924
	0.020	3.251	6.451	5.255
	0.040	3.774	Stable	9.067
A_y (m)	0.000	0.834	0.834	0.824
	0.006	0.822	0.748	0.771
	0.010	0.815	0.699	0.732
	0.020	0.795	0.503	0.616
	0.040	0.753	Stable	Stable
A_z (m)	0.000	0.081	0.093	0.083
	0.006	0.079	0.081	0.076
	0.010	0.079	0.074	0.071
	0.020	0.076	0.049	0.057
	0.040	0.071	Stable	Stable
A_θ (deg.)	0.000	2.638	2.626	2.655
	0.006	2.595	2.294	2.447
	0.010	2.565	2.108	2.294
	0.020	2.490	1.410	1.853
	0.040	2.328	Stable	Stable

Table 4.4 Results for the line having three hybrid dampers and undergoing two loops per span galloping

$\xi = 0$, 0.006, 0.01, 0.02 and 0.04

Span length L_x : 200m
Mass of each hybrid damper: 5kg
Locations of hybrid dampers: $L_x/4$, $5L_x/12$, $2L_x/3$

Horizontal Tension H: 30kN
Wind speed U_z: 9m/s
$\alpha_{static} = 40^0$

Two loops per span	ξ	Values of the frequency ratio $\omega_y / \omega_{\theta d}$		
		0.90	1.00	1.10
Critical wind speed (m/s)	0.000	3.088	2.969	3.119
	0.006	3.743	5.343	4.625
	0.010	4.204	6.187	5.780
	0.020	5.472	7.845	10.160
	0.040	9.135	9.587	26.797
A_y (m)	0.000	0.550	0.192	0.538
	0.006	0.510	0.191	0.447
	0.010	0.481	0.185	0.371
	0.020	0.397	0.147	Stable
	0.040	Stable	Stable	Stable
A_z (m)	0.000	0.245	1.033	0.211
	0.006	0.225	0.902	0.170
	0.010	0.210	0.835	0.138
	0.020	0.169	0.612	Stable
	0.040	Stable	Stable	Stable
A_θ (deg.)	0.000	3.141	7.264	3.065
	0.006	2.883	6.123	2.486
	0.010	2.697	5.568	2.013
	0.020	2.168	3.916	Stable
	0.040	Stable	Stable	Stable

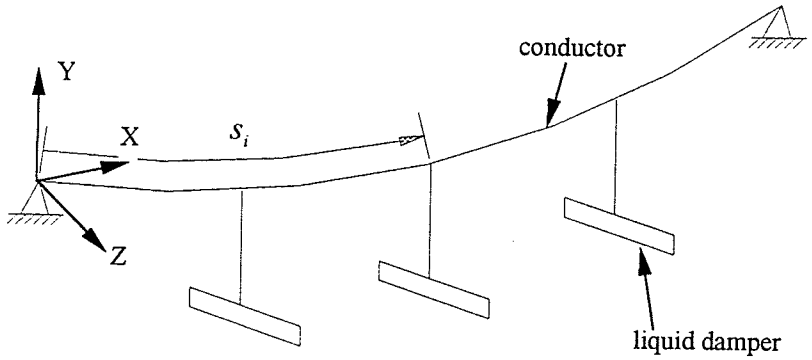

(a)

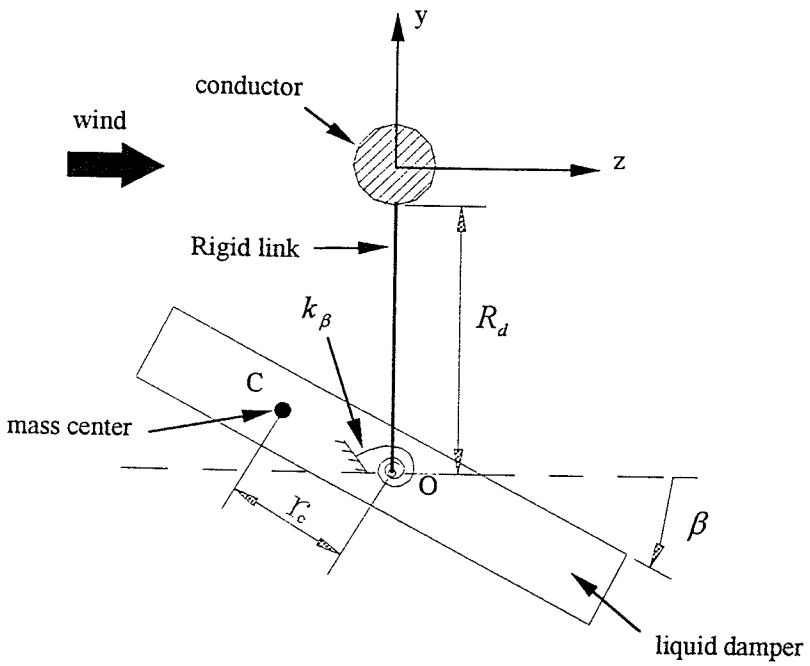

(b)

Figure 4.1. Showing (a) a transmission line having hybrid dampers, and (b) conceptual details of a hybrid damper.

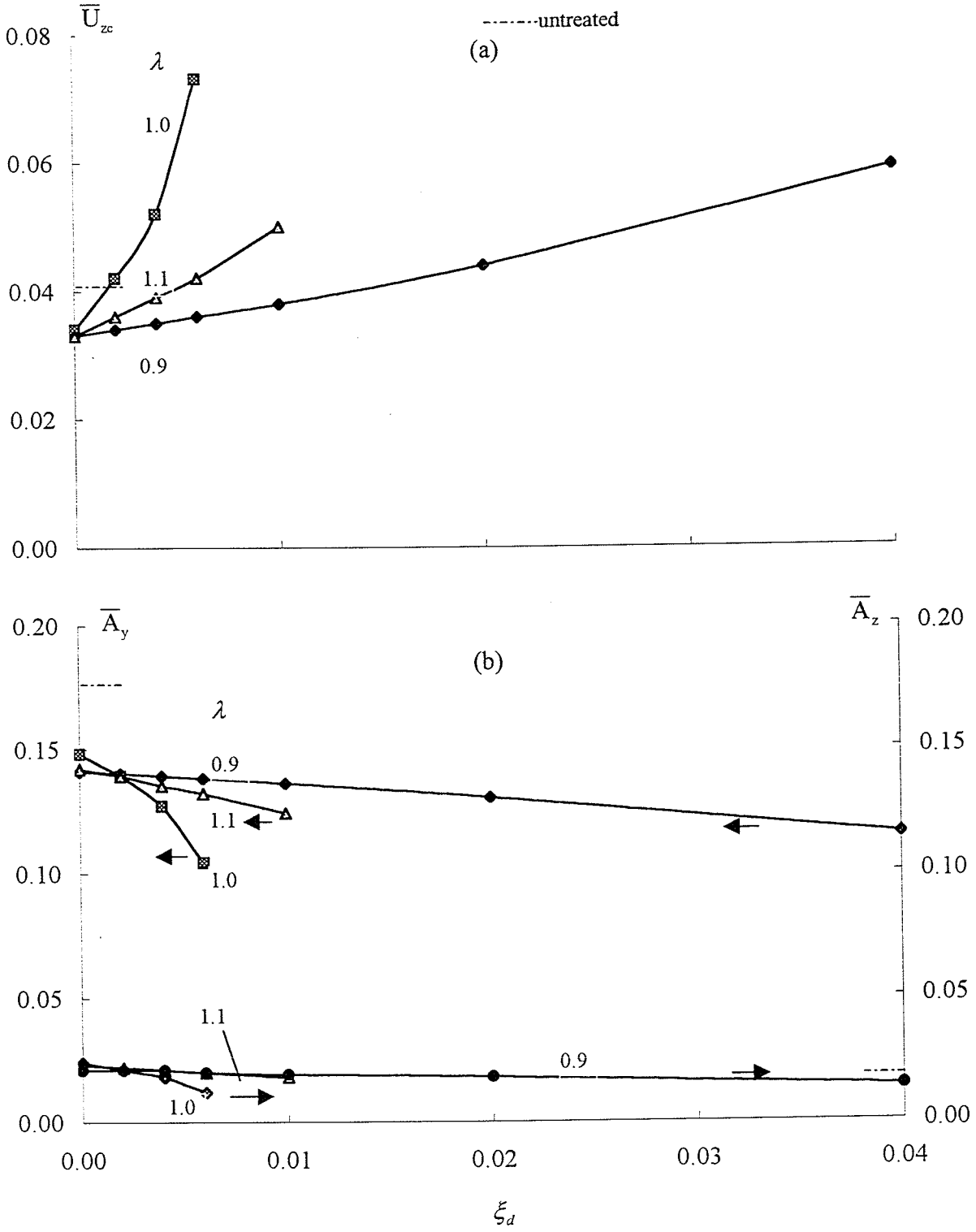

Figure 4.2. Showing $\overline{U}_{zc}$, $\overline{A}_y$ and $\overline{A}_z$ for different ξ . One hybrid damper is located at the mid-span and 1 loop per span galloping may occur. H=30kN, Lx=200m and Uz=9m/s.

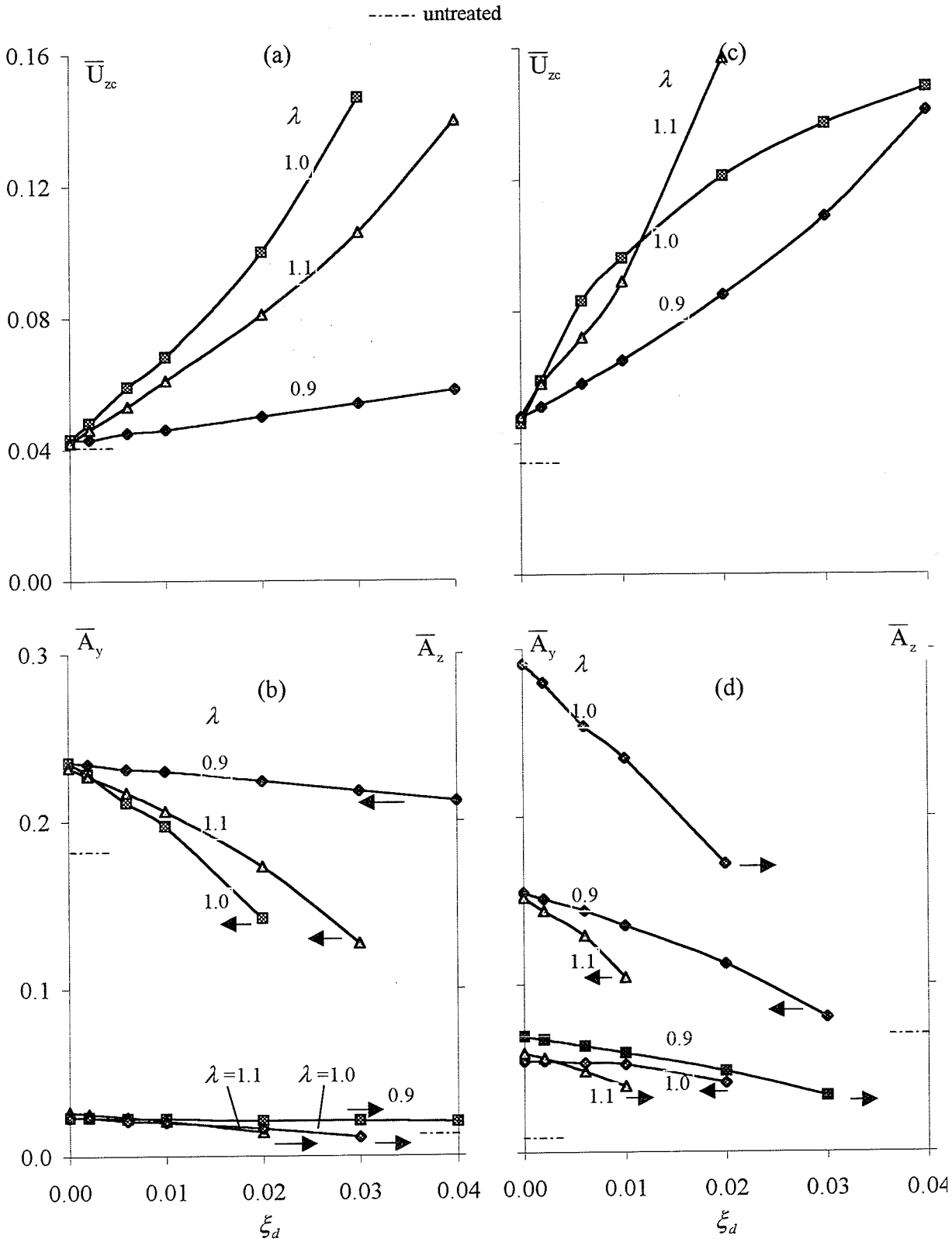

Figure 4.3. Showing $\overline{U}_{zc}$, $\overline{A}_y$ and $\overline{A}_z$ for different ξ and three hybrid dampers. (a), (b) 1 loop per span and (c), (d) 2 loops per span galloping. H=30kN, Lx=200m and U_z=9m/s.

Chapter 5

CONCLUSIONS

A generalized 3DOF hybrid model has been developed to describe the motions of an iced single or bundle conductor for which interactions between the vertical, horizontal and torsional motions are allowed. This model is an extension to a bundle conductor of a previous single conductor model but still includes closed-form expressions for the initiation stability, limit cycles and their stability conditions. In addition, the hybrid model couples FE mode shapes to analytical expressions so that the model can handle practical spatial variations of nonuniform icing and structural damping. It is impossible for a general analytical model to consider such cases. Numerical examples have shown that the hybrid model generates results that agree with those of a FE model which has also been extended to a bundle having any number of conductors.

A parametric analysis is required for the design of a new transmission line. The quite efficient hybrid model can economically compute the effects of design changes in parameters like the static tension, the span length and number of conductors in a bundle or the result of a greater wind speed. It makes possible the optimum selection of parameters.

The final objective in studying the galloping of an electrical transmission line is to control the galloping itself. The hybrid model accommodates control devices like airflow spoilers, detuning pendulums and hybrid dampers. Consequently, it can be used to investigate the effects of these control devices on galloping and provide guidelines for their design.

Computer software has been developed on the basis of the hybid model. It saves substantial computational time compared with the time integration methods used in many analytical models. It can give predictions almost instantenously on a personal computer because explicit

expressions are used. Moreover, it conveniently provides inital (guess) values for the FE software. Therefore, the hybrid model can be used as an effective tool for a galloping analysis and the design of an electrical transmission line.

References

[1] J. P. Den Hartog (1932). "Transmission line vibration due to sleet." *AIEE Transactions*, Vol. 51, pp. 1074 – 1076.

[2] Transmission Line Reference Book (1979). "Wind - induced conductor motion." *EPRI*, Palo Alto, California.

[3] P. Yu, A. H. Shah and N. Popplewell (1992). "Initially coupled galloping of iced conductors." *Journal of Applied Mechanics*, ASME 59 (1), 140 – 145.

[4] A. T. Edwards and A. Madeyski (1956). "Progress report on the investigation of galloping of transmission line conductors." *Trans. AIEE*, 75(3), 666 – 686.

[5] O. Nigol and O. G. Buchan (1981). "Conductor galloping : Torsional mechanism – Parts I and II." *Tr. IEEE*, PAS – 96 (2), 699 – 720.

[6] J. J. Ratkowski (1963). "Experiments with galloping spans." *IEEE Trans. PAS*, Vol. 82, 661 – 667.

[7] J. Chadha (1974). "A study of the mechanisms of conductor galloping and its control." *Ontario Hydro Research Division Report*, No.74 – 212 – k.

[8] C. B. Rawlin (1991). "Galloping stability of a single conductor with electricity research laboratories' wet snow shape 2." *Alcoa Conductor Products Company*, Tech Note No. 29.

[9] R. D. Blevins and W. D. Iwan (1974). "The galloping response of a two-degree-of-freedom system." *ASME, Journal of Applied Mechanics*, 41, 1113 – 1118.

[10] D. A. Davis, D. J. W. Richards and R. A. Scriven (1963). "Investigation of conductor oscillations on the 275 kV crossing over the rivers Severn and Wye." *Proc. IEE*, Vol. 110(1), 205 – 219.

[11] A. Simpson (1965). "Aerodynamic instability of long-Span transmission lines," *Proc. IEE*, Vol. 112(2), 315 – 324.

[12] K.F. Jones (1992). "Coupled vertical and horizontal galloping." *Journal of Engineering Mechanics, ASCE*, 118(1), 92 – 107.

[13] Manitoba Hydro (1992). "Modelling of conductor galloping." *Canadian Electrical Association Report*, Vol I & II, Project No. 321 T 672, Montreal, Canada.

[14] Manitoba Hydro (1995). "Modelling of conductor galloping." *Canadian Electrical Association Report*, Phase II, Project No. 321 T 672A, Montreal, Canada.

[15] P. Yu, Y. M. Desai, A. H. Shah and N. Popplewell (1993). "Three-degree-of-freedom model for galloping, (Part I and II)." *Journal of Engineering Mechanics*, ASCE, 119 (12), 2405 – 2448.

[16] P. C. M. Gortemaker (1984). "Galloping conductors and evaluation of the effectiveness of inspan dampers." *Kema Science and Technical Reports*, Netherlands, 2(4), 27 – 39.

[17] P. Yu, N. Popplewell and A. H. Shah (1991). "A geometrical approach assessing instability trends for galloping." *Journal of Applied Mechanics*, 58(3), 784 – 791.

[18] P. Yu, N. Popplewell and A. H. Shah (1995). "Instability trends of inertially coupled galloping, part I: initiation." *Journal of Sound and Vibration*, 183(4), 679 – 691.

[19] P. Yu, N. Popplewell and A. H. Shah (1995). "Instability trends of inertially coupled galloping, partII: periodic vibrations." *Journal of Sound and Vibration*, 183(4), 697 – 691.

[20] A. S. Richardson, Jr. (1988). "Bluff body aerodynamics." *ASCE, Journal of Structural Engineering*. Vol. 112(7), 1723 – 1726.

[21] W. T. Vanhorssen (1987). "Asymptotics for a system of nonlinearly coupled wave equations with an application to the galloping oscillation of overhead transmission lines." *Technische Hogeschool Delft*, Netherland, Rept. No. REPT – 87 – 78.

[22] Y. M. Desai (1991). "Modelling of planar transmission line galloping." *Ph.D Thesis*, University of Manitoba.

[23] G. Adomian (1987). "Nonlinear oscillations in physical system." *Mathematics and Computers in Simulation*, Vol. 29, 784 – 791.

[24] G. Chen (1987). "Applications of a generalized Galerkin's method to non-linear oscillations of two-degree-of-freedom system." *Journal of Sound Vibration*. Vol. 119(2), 225 – 242.

[25] G. S. Byun and R. I. Egbert (1991). "Two-degree-of-freedom analysis of power line galloping by describing function method." *Electric power System Research*, 21(3), 187 – 193.

[26] A. S. Richardson, Jr. (1981). "Dynamic analysis of lightly iced conductor galloping in two degrees of freedom." *Proc. IEEE*, 128 (Pt. C)(4), 211 – 218.

[27] A. S. Richardson (1991). "A study of galloping conductors on a 230KV transmission line." *Electric Power System Research*, 21, 43 – 55.

[28] R. D. Blevins (1990). "Flow – induced vibration (2nd edition)." *Van Nostrand Reinhold Co.*, New York.

[29] Y. Nakamura (1980). "Galloping of bundled power line conductors." *Journal of Sound and Vibration*, Vol.73, No.3, 363 – 377.

[30] W. Jianwei (1996). "Large vibrations of overhead electrical lines." *Ph.D Thesis*, Universite De Liege, Belgium.

[31] A. Simpson (1974). "Determination of the natural frequencies of multiconductor overhead transmission lines." *Journal of Sound and Vibration*, Vol.20, No.4, 417 – 449.

[32] G. Diana, F. Cheli, A. Manenti, P. Nicolini and F. Tavano (1990). "Oscillation of bundle conductors in overhead lines due to turbulent wind." *IEEE Transaction on Power Delivery*, 5(4), 1910 – 1919.

[33] K. E. Gawronski (1977). "Non-linear galloping of bundle-conductor transmission lines." *Ph.D Thesis*, Clarkson College of Technology.

[34] Y. M. Desai, P. Yu, N. Popplewell and A. H. Shah (1996). "Perturbation-based finite element analyses of transmission line galloping." *Journal of Sound and Vibration*, 191(4), 469 – 489.

[35] M. Liao (1996). "Galloping of bundle transmission lines." *Ph.D Thesis*, University of Manitoba, Winnipeg, Canada.

[36] A. N. Shealy, K. L. Althouse and R. N. Youtz (1952). "Forty-two years' experience combating sleet accumulations." *AIEE Transactions*, Vol.52, 621 – 628.

[37] J. E. Clem (1930). "Currents required to remove conductor 'sleet'." *Electrical World*, December 6, 1053 – 1056.

[38] A. E. Davison (1939). "Ice-coated electrical conductor." *Bulletin, Hydro-Electric Power Commission of Ontario*, Vol.26, No.9, September, 271 – 280.

[39] K. Anjo, S. Yamasaki, Y. Matsubayashi, Y. Nakayama, A. Otsuki and T. Fujimura (1974). "An experimental study of bundle conductor galloping on the Kasatori-Yama test line for bulk power transmission." *CIGRE Report*, 22 – 04.

[40] C. J. Pon (1988). "Control of distribution line galloping." *Canadian Electrical Association Report*, No. 133 – T – 386, Toronto, Canada.

[41] C. J. Pon and D. G. Harvard (1990). "Field trials of galloping control devices for bundle conductor lines." *Canadian Electrical Association Report*, No. 133 – T – 386, Toronto, Canada.

[42] D. G. Harvard and C. J. Pon (1990). "Use of detuning pendulums for control of galloping of single conductor and two and four conductor transmission lines." *Transactions of the 5th Int. Workshop on the Atmospheric Icing of Structures*, Tokyo, Japan.

[43] A. S. Richardson (1962). "Galloping conductors-progress toward a practical solution of the problem." *EEI Bulletin*, Vol.30, No.5.

[44] A. S. Richardson, Jr. (1968). "Design and performance of an aerodynamic anti-galloping device." *IEEE Conference Paper*, C68670 – PWR.

[45] D. G. Harvard, C. J. Pon and J. C. Pohlman (1986). "Reduction of tower head dimensions through galloping controls." *Proc. of the 3th Int. Workshop on the Atmospheric Icing of Structures*, Vancouver, Canada, 441 – 449.

[46] P. Hagedorn (1982). "Non-linear oscillations." *Clarendon Press*, Oxford.

[47] R. W. Clough and J. Penzien (1975). "Dynamics of structures." *McGraw – Hill*, New York.

[48] Y. M. Desai, N. Popplewell, A. H. Shah and D. N. Buragohain (1988). "Geometric nonlinear static analysis of cable supported structures." *Computers and Structures*, 29(6), 1001 – 1009.

[49] K.G. Mcconnell and C. N. Chang (1986). "A study of the axial-torsional coupling effect on a sagged transmission line." *Experimental Mechanics*, 26(4),324 – 329.

[50] P. Stumpf (1994). "Determination of aerodynamic forces for iced single and twin–bundled conductors." *M. Sc. Thesis*, University of Manitoba, Winnipeg, Canada.

[51] Y. M. Desai, P. Yu, N. Popplewell and A. H. Shah (1995). "Finite element modelling of transmission line galloping." *Computers and Structures*, Vol.57, No.3, 469 – 489.

[52] A. S. Veletsos and G. R. Darbre (1983). "Dynamic stiffness of parabolic cables." *International Journal of Earthquake Engineering and Structural Dynamics*, 11, 367 – 401.

[53] R. K. Mathur, A. H. Shah, P. G. S. Trainor and N. Popplewell (1987). "Dynamics of a guyed transmission tower system." *IEEE*, Trans. PWRD, Power Delivery, 2(3), 908 – 916.

[54] D. G. Havard (1978). "Galloping control by detuning." *Progress Report* No. 1, Ontario Hydro, Canada.

Appendix A

ELEMENTS OF M, $\mathbf{K}_a$ and F

A.1 Mass matrix, M

The representative elements, m_{ij} $(i,j = 1,2,3)$, of the symmetrical mass matrix, **M**, that appear in equation (3.14) are

$$\begin{aligned} m_{11} &= \int_0^L \int_{A_T} \rho dA f_v^2 ds + \sum_{k=1}^{p} m_{sk} f_v^2(s_k) \ , \\ m_{22} &= \int_0^L \int_{A_T} \rho dA f_w^2 ds + \sum_{k=1}^{p} m_{sk} f_w^2(s_k) \ , \qquad \text{(A.1)} \\ m_{33} &= \int_0^L \int_{A_T} \rho(y^2+z^2) dA f_\theta^2 ds + \sum_{k=1}^{p} I_{sk} f_\theta^2(s_k) \ , \qquad \text{(A.2)} \\ m_{13} &= -\int_0^L \int_{A_T} \rho z dA f_v f_\theta ds \qquad \text{(A.3)} \end{aligned}$$

and

$$m_{23} = \int_0^L \int_{A_T} \rho y dA f_w f_\theta ds \ . \qquad \text{(A.4)}$$

A.2 Stiffness matrix, $\mathbf{K}_a$

The representative elements, K_{ij} $(i,j = 1,2,3,4)$, of the symmetrical stiffness matrix, $\mathbf{K_a}$, in equation (3.13) are obtained by summing on each conductor k $(k = 1 \sim n)$ as

$$\begin{aligned} K_{ij} &= \sum_{k=1}^{n} D_{ij} \int_0^L \beta_i \beta_j f_{i,s} f_{j,s} ds - n_2 K_{ice} + n_3 \sum_{k=1}^{n} H_k \int_0^L \frac{\partial s}{\partial x} f_{i,s} f_{j,s} ds \\ &+ n_4 \sum_{k=1}^{n} (AE)_k \int_0^L \beta_i f_{i,s} Q_k ds - n_5 \sum_{k=1}^{n} H_k \int_0^L \frac{\partial s}{\partial x} f_{i,s} Q_{2k} ds \\ &+ n_6 \sum_{k=1}^{n} H_k \int_0^L \frac{\partial s}{\partial x} f_{i,s} Q_{1k} ds + 2 n_7 B_T \sum_{k=1}^{n} \int_0^L f_{4,s} Q_k ds \end{aligned}$$

$$+n_7(\sum_{k=1}^{n} H_k \int_0^L \frac{\partial s}{\partial x} f_{i,s}^2 r_k^2 ds + \sum_{k=1}^{n} (AE)_k \int_0^L Q_k^2 ds)$$
$$+K_x(f_u^2(0) + f_u^2(L)) \tag{A.5}$$

where

$$D_{ij} = (AE)_k \qquad for\ all\ i\ and\ j\ other\ than\ 4\ ,$$

$$D_{ij} = B_T \qquad for\ i = 4\ or\ j = 4,\ i \neq j\ ,$$

$$D_{ij} = (GJ)_k \qquad for\ i = j = 4\ ,$$

$$f_{i,s} = \frac{\partial f_i}{\partial s},\quad \beta_1 = \frac{\partial x}{\partial s},\quad \langle \beta_2, \beta_3 \rangle = \langle \frac{\partial y}{\partial s}, \frac{\partial z}{\partial s} \rangle,\quad \beta_4 = 1\ , \tag{A.6}$$

and

$$\begin{aligned} Q_k &= \beta_3 Q_{1k} - \beta_2 Q_{2k}, \\ Q_{1k} &= r_k \cos\theta_{k0} f_{4,s}, \\ Q_{2k} &= r_k \sin\theta_{k0} f_{4,s}. \end{aligned} \tag{A.7}$$

Moreover,

$$n_2 = \begin{cases} 1 & i = j = 4 \\ 0 & otherwise\ , \end{cases} \qquad n_3 = \begin{cases} 1 & i = j = 1,\ 2,\ 3 \\ 0 & otherwise, \end{cases}$$

$$n_4 = \begin{cases} 1 & i \leq 3,\ \ j = 4 \\ 0 & otherwise\ , \end{cases} \qquad n_5 = \begin{cases} 1 & i = 2,\ \ j = 4 \\ 0 & otherwise\ , \end{cases}$$

$$n_6 = \begin{cases} 1 & i = 3,\ j = 4 \\ 0 & otherwise\ , \end{cases} \qquad n_7 = \begin{cases} 1 & i = j = 4 \\ 0 & otherwise\ . \end{cases} \tag{A.8}$$

Here, $i, j = 1, 2, 3, 4$ represent $i, j = u, v, w, \theta$ for convenience; H is the horizontal component of a conductor's static tension, T; and K_{ice}, which is the stiffness due to the eccentric ice, is [16]

$$K_{ice} = \int_0^L (\int_{A_T} \rho y dA) g f_\theta^2 ds\ . \tag{A.9}$$

Furthermore, K_x is the stiffness due to the static coupling of the span of interest with its adjacent spans and insulator strings It is given by [52, 53]

$$K_x = \sum_{i=1}^{n}\left(\frac{12(AE)_i H_i^3}{12LH_i^3 + (AE)_i p_{yi}^2 L_x^3} + \frac{p_{yi}L}{L_i} + \frac{W_i}{2L_i}\right) . \tag{A.10}$$

L_x is the horizontal distance between adjacent towers; p_{yi} is the total vertical load per unit length of the ith conductor whereas W_i and L_i are the total weight and length of the insulator string, respectively.

A.3 Aerodynamic load, F

The elements of the aerodynamic load vector, **F**, used in equation (3.15) are

$$F_y = \frac{1}{2}\rho_{air} U_z^2 dC_y , \tag{A.11}$$

$$F_z = \frac{1}{2}\rho_{air} U_z^2 dC_z \tag{A.12}$$

and

$$F_\theta = \frac{1}{2}\rho_{air} U_z^2 d^2 C_\theta \tag{A.13}$$

where

$$\begin{aligned} C_y &= f_{v\theta}(A_{y_1}\alpha' + A_{y_2}\alpha'^2 + A_{y_3}\alpha'^3) , \\ C_z &= A_{z_1}\alpha' + A_{z_2}\alpha'^2 + A_{z_3}\alpha'^3 , \\ C_\theta &= A_{\theta_1}\alpha' + A_{\theta_2}\alpha'^2 + A_{\theta_3}\alpha'^3 , \end{aligned} \tag{A.14}$$

$$f_{v\theta} = \frac{2}{L}\int_0^L f_v f_\theta ds , \tag{A.15}$$

$$\alpha' = q_\theta - \frac{d}{2U_z}\dot{q}_\theta - \frac{f_{v\theta}}{U_z}\dot{q}_v = \alpha f_\theta \tag{A.16}$$

and

$$A_{ij} = \int_0^L a_{ij} f_\theta^{j+1} ds \qquad i = y, z, \theta, \quad j = 1, 2, 3 . \tag{A.17}$$

The aerodynamic coefficients, a_{ij}, are obtained by curve-fitting experimental, quasi-steady wind loads in the neighborhood of the initially twisted conductor's profile sustained by the moment

arising from the eccentric ice weight [50]. The lift and drag coefficients, C_L and C_D, respectively, are given by

$$C_L = C_y \cos\alpha - C_z \sin\alpha \tag{A.18}$$

and

$$C_D = C_y \sin\alpha + C_z \cos\alpha. \tag{A.19}$$

Appendix B

ELEMENTS OF $\mathbf{M}_d$, $\mathbf{K}_d$ and $\mathbf{C}_d$

B.1 Mass matrix, $\mathbf{M}_d$

The representative elements, $m_{d_{ij}}$ $(i,j=1,2,3)$, of the symmetric mass matrix, $\mathbf{M}_d$, are

$$m_{d_{11}} = \sum_{k=1}^{n_m}\{m_{d_k}[f_v^2(s_k) - 2r_{c_k}f_v(s_k)\beta_{v_k}] + I_{o_k}\beta_{v_k}^2\}\ , \tag{B.1}$$

$$m_{d_{22}} = \sum_{k=1}^{n_m}\{m_{d_k}f_w^2(s_k) + I_{o_k}\beta_{w_k}^2\}\ , \tag{B.2}$$

$$m_{d_{33}} = \sum_{k=1}^{n_m}\{m_{d_k}R_k^2 f_\theta^2(s_k) + I_{o_k}\beta_{\theta_k}^2\}\ , \tag{B.3}$$

$$m_{d_{12}} = \sum_{k=1}^{n_m}\{I_{o_k}\beta_{v_k}\beta_{w_k} - m_{d_k}r_{c_k}f_v(s_k)\beta_{w_k}\}\ , \tag{B.4}$$

$$m_{d_{13}} = \sum_{k=1}^{n_m}\{I_{o_k}\beta_{v_k}\beta_{\theta_k} - m_{d_k}r_{c_k}f_v(s_k)\beta_{\theta_k}\}\ , \tag{B.5}$$

and

$$m_{d_{23}} = \sum_{k=1}^{n_m}\{I_{o_k}\beta_{w_k}\beta_{\theta_k} - m_{d_k}R_{d_k}f_w(s_k)f_\theta(s_k)\}\ . \tag{B.6}$$

B.2 Stiffness matrix, $\mathbf{K}_d$

The representative elements, k_{ij} $(i,j=1,2,3)$, of the symmetrical stiffness matrix, $\mathbf{K}_d$, which appears in equation (4.7) are

$$k_{11} = \sum_{k=1}^{n_m} k_{\beta_k}\beta_{v_k}^2 \qquad k_{12} = \sum_{k=1}^{n_m} k_{\beta_k}\beta_{v_k}\beta_{w_k} \qquad k_{13} = \sum_{k=1}^{n_m} k_{\beta_k}\beta_{v_k}\beta_{\theta_k} \tag{B.7}$$

and

$$k_{22} = \sum_{k=1}^{n_m} k_{\beta_k}\beta_{w_k}^2 \qquad k_{23} = \sum_{k=1}^{n_m} k_{\beta_k}\beta_{w_k}\beta_{\theta_k} \qquad k_{33} = \sum_{k=1}^{n_m}\{k_{\beta_k}\beta_{\theta_k}^2 + m_{d_k}gR_{d_k}\}\ . \tag{B.8}$$

B.3 Damping matrix, $\mathbf{C}_d$

The diagonal damping matrix, $\mathbf{C}_d$, is constructed by neglecting the damping coupling in different directions. Its elements can be expressed as

$$c_{d_{11}} = \sum_{k=1}^{n_m} c_{\beta_k} \beta_{v_k}^2 \qquad c_{d_{22}} = \sum_{k=1}^{n_m} c_{\beta_k} \beta_{w_k}^2 \qquad c_{d_{33}} = \sum_{k=1}^{n_m} c_{\beta_k} \beta_{\theta_k}^2 \ . \tag{B.9}$$